Energy Conversion and Management 369 (2026) 122054

Contents lists available at ScienceDirect

Energy Conversion and Management

journal homepage: www.elsevier.com/locate/enconman

Multi-objective optimisation of renewable energy integration in circular brine valorisation/treatment: The case of the CARMEn chain

Stefania Guarino *, Pietro Catrini, Giuseppe Battaglia, Giuseppe Scelfo, Giorgio Maria Micale, Livan Fratini

University of Palermo, Department of Engineering, Viale delle Scienze, 90128 Palermo, PA, Italy

ARTICLE INFO

Keywords:
Brine valorisation
Circular desalination
Photovoltaic-thermal hybrid system
Battery storage
Multi-objective optimisation
NSGA-II
Techno-economic assessment
CO_2 emissions

ABSTRACT

Circular brine-valorisation chains offer a promising route to address water scarcity and critical raw-material recovery, but their large electrical and thermal energy demands can offset environmental benefits if powered by fossil sources. This work develops a fully integrated, hourly resolved simulation and multi-objective optimisation framework for the CARMEn treatment chain – combining nanofiltration, $Mg(OH)_2$ precipitation, softening, electrodialysis with bipolar membranes, membrane distillation and reverse electrodialysis – coupled with a hybrid solar energy system comprising photovoltaic panels, lithium-ion battery storage, flat-plate solar-thermal collectors and a hot-water storage tank. Three representative brine feeds are analysed at a saltwork site in Trapani (Italy): reverse-osmosis brine, nanofiltration retentate and saltwork bittern, each targeting 50 t/y of $Mg(OH)_2$ production. A deterministic Python model computes 8760 h energy balances, system dispatch, discounted cash flows and operational CO_2 emissions. A multi-objective genetic optimisation algorithm explores the trade-offs between net present value, electrical and thermal coverage, and capital expenditure. Results show that all scenarios are economically viable at baseline market conditions (net present value of 224–277 k€, internal rate of return of 11–11.5 %, payback of about 8 years), with nanofiltration retentate achieving the best economic performance. Bittern attains comparable renewable shares (electrical coverage of 54 %, thermal coverage of 74 %) at the lowest capital expenditure (514 k€). Sensitivity analysis identifies the electricity export tariff as the primary economic driver, while battery capital cost governs storage sizing, with an economic break-even threshold around 150 €/kWh. Avoided CO_2 emissions range from 37.8 t/y for bittern to 85.4 t/y for reverse-osmosis brine, with the thermal contribution dominating in heat-intensive scenarios. The proposed framework provides a systematic tool for the co-design of solar-powered circular brine-valorisation systems, with the specific quantitative results reflecting the solar resource and regulatory context of the Trapani case study considered here.

1. Introduction

Freshwater scarcity is intensifying worldwide due to climate change, population growth, groundwater depletion and the increasing frequency of extreme climatic events. He et al. [1] project that global urban water scarcity will intensify substantially in the coming decades and identify technological and infrastructural interventions as key mitigation levers. Consistently, Eke et al. [2] document the rapid global expansion of desalination capacity and technology deployment as a central strategic response to water stress. However, while desalination effectively addresses water scarcity, it simultaneously generates large volumes of hypersaline reject streams whose management poses environmental and economic concerns. Brine streams typically exhibit salinity levels significantly higher than those of seawater and may contain chemical additives such as antiscalants and disinfectants, depending on intake-water quality and pre-treatment conditions [3]. Deep-well injection can be an effective solution for inland desalination plants, as it isolates brine in deep confined geological formations, but its feasibility is strongly site-specific and must ensure protection of groundwater resources [4]. Surface discharge is still the most common practice worldwide and, when properly designed and monitored, can be environmentally acceptable. However, uncontrolled releases may cause local salinity and temperature increases (up to 30–40 °C); Omerspahic et al. [5] document such impacts on marine chemistry and ecosystem health in detail. In response to these documented risks, Panagopoulos

* Corresponding author.
E-mail address: stefania.guarino@unipa.it (S. Guarino).

https://doi.org/10.1016/j.enconman.2026.122054
Received 12 May 2026; Received in revised form 6 August 2026; Accepted 10 August 2026
0196-8904/© 2026 The Author(s). Published by Elsevier Ltd. This is an open access article under the CC BY license (http://creativecommons.org/licenses/by/4.0/).

Nomenclature

Symbols

a	the empirically-determined coefficient that accounts for convective heat losses at near-stagnant air conditions
a_1	the first-order heat loss coefficient [W/(m^2·K)] [Eq. (14)]
A_{coll}	the total solar-thermal field area [m^2]
b	the empirically-determined coefficient that accounts for the influence of wind on the thermal losses [Eq. (2)]
B_y	the yearly economic benefit [€/y]
c_{batt}	the unit investment cost of the battery [€/kWh]
C_{batt}	the nominal battery energy capacity [kWh]
c_{boiler}	the unit investment cost of the gas boiler [€/kW]
$C_{CO_2,y}$	the monetized carbon benefit [€/y]
c_{coll}	the unit investment cost of the solar-thermal field [€/m^2]
C_{el}	the electrical self-sufficiency fraction [%]
$C_{gas,y}$	the annual gas boiler fuel cost [€/y]
c_{grid}	the electricity retail price [€/kWh]
c_{PV}	the unit investment cost of PV system [€/kWp]
c_{th}	the thermal energy cost [€/kWh]
C_{th}	the thermal self-sufficiency fraction [%]
$c_{th,store}$	the unit investment cost of the thermal storage [€/kWh]
C_{tot}	the total investment cost [€]
$D_{fut}(t)$	the anticipated net energy deficit over the look-ahead horizon [kWh]
$E_{batt\rightarrow L}$	the electricity delivered to the load from the battery [kWh$_e$]
$E_{exp,y}$	the annual exported electrical energy [kWh$_e$/y]
$E_{imp,y}$	the residual annual electricity imported from the grid [kWh$_e$]
$E_{load,y}$	the annual electrical energy demand [kWh$_e$]
E_{max}	the maximum energy that can be stored in the battery [kWh$_e$]
$E_{PV\rightarrow batt}(t)$	the energy directed from PV to battery charging at timestep t [kWh]
$E_{PV\rightarrow L}(t)$	the energy directed from PV to load at timestep t [kWh]
E_{res}	resilience reserve energy of the battery [kWh]
$E_{room}(t)$	is the available SOC headroom at time t [kWh]
$E_{self,y}$	the annual electrical energy served on site (by PV and battery) [kWh$_e$/y]
$E_{SOC}(t)$	the instantaneous stored energy [kWh]
$E_{target}(t)$	the dynamic minimum SOC target of the battery [kWh]
$E_{th,store}$	the energy capacity of the thermal storage [kWh]
EF_{el}	the emission factors associated with the national electrical grid [kgCO$_2$/kWh]
EF_{th}	the emission factors associated with an efficient natural gas-boiler [kgCO$_2$/kWh]
G_b	the beam component of the global solar irradiance [W/m^2]
$G_{d,Hay-Davies}$	the diffuse component from the Hay-Davies model [W/m^2]
G_{POA}	the total in-plane irradiance [W/m^2]
G_r	the ground-reflected irradiance [W/m^2]
L	the aggregate PV system loss factor [%]
$L_{fut}(t)$	the cumulative future electrical demand over the horizon of 12h [kWh]
LCOMg	Levelized Cost of Mg(OH)$_2$ [€/kg]
$M_{CO_2,y}$	the annual avoided emissions [kgCO$_2$/y]
N	the project lifetime in years [y]
N_{cycles}	the equivalent number of full charge–discharge battery cycles per year [y^{-1}]
OM_y	the annual operation and maintenance cost [€/y]
$P_{AC,net}$	the AC output PV power [W]
p_c	the crossover probability [-]
p_{CO_2}	the constant carbon price [€/tCO$_2$]
P_{DC}	the DC output power [W]
$P_{DC,0}$	the nominal DC power at reference conditions [W]
p_m	the mutation probability [-]
$P_L(t)$	the instantaneous electrical load [kW]
$\overline{P}_L$	the scenario mean electrical load [kW]
$P_{PV}(t)$	the instantaneous photovoltaic power generation [kW]
$p_{SSP}(t)$	the hourly grid export remuneration [€/kWh]
$P_{th}(t)$	the thermal power generated at timestep t from solar field [kW]
$PV_{fut}(t)$	the cumulative future PV generation over the horizon of 12h [kWh]
$Q_{boiler,y}$	the thermal energy not covered by the solar subsystem at year y [kWh/y]
$Q_{sol,y}$	the useful thermal energy delivered by the solar subsystem [kWh]
$Q_{th,load,y}$	the annual thermal load [kWh$_{th}$]
r	the real discounted rate [-]
R_y	the cost of optional reinvestments [€/y]
$S(t)$	the net power surplus or deficit [kW]
SOC_{max}	the maximum state-of-charge fraction of the battery [-]
SOC_{min}	the hard lower bound of battery state-of-charge [-]
$SOC_{reserve}$	the minimum state-of-charge fraction of the battery retained for instantaneous blackout events [-]
T_a	the ambient temperature [°C]
t_{aut}	the required autonomy horizon [h]
T_{cell}	the solar cell temperature [°C]
$T_{feed,in}$	the inlet temperature of the feed stream into the chain [°C]
$T_{feed,out}$	the outlet temperature of the feed stream from the chain [°C]
T_m	the PV module operating temperature [°C]
$T_{mean}(t)$	the mean fluid temperature in the solar collector [°C]
v_w	the wind speed [m·s^{-1}]
$\mathbf{x}$	the vector of the decision variables of the optimisation problem

Greek letters

γ	the temperature coefficient of DC output power [°C^{-1}]
δ_{PV}	the PV degradation rate [%/y]]
ΔT	the reference temperature difference between the cell and the module back surface [°C]
ϑ_i	the solar incidence angle [°]
φ_y	the annual derating factor applied to PV-derived energy [-]
η_0	the optical efficiency of the collector at reference conditions [%]
η_c	the distribution index of the Simulated Binary Crossover (SBX) operator [-]
η_{ch}	the charging battery efficiency [%]
η_{coll}	the instantaneous solar collector efficiency [%]
η_{dis}	the discharging battery efficiency [%]
η_{inv}	the efficiency of the inverter model [%]
η_m	the distribution index of the polynomial mutation operator [-]
η_{rt}	the round-trip efficiency of the electrical/thermal storage system [%]
σ	the mutation scale factor [-]

Acronyms

AGMD	Air-Gap Membrane Distillation
BOS	Balance of System
CAPEX	Capital Expenditure
CARMEn	A novel Circular Approach to Recover Critical Raw Materials and Energy from Spent Seawater Brines
CHP	Combined Heat and Power
CPV	Concentrator Photovoltaic
CRM	Critical Raw Materials

DC/AC	Direct/Alternating Current	NF	Nanofiltration
DCMD	Direct-Contact Membrane Distillation	NPV	Net Present Value
DHI	Diffuse Horizontal Irradiance	NSGA	Non-dominated Sorting Genetic Algorithm
DHW	Domestic Hot Water	O&M	Operation and Maintenance
DNI	Direct Normal Irradiance	POA	Plane-of-Array
DPBT	Discounted Payback Time	PUN	Prezzo Unico Nazionale
EDBM	Electrodialysis with Bipolar Membranes	PV	Photovoltaic
FR	Fully Renewable	PVGIS	Photovoltaic Geographical Information System
GC	Grid Connected	PVPS	Photovoltaic Power Systems Programme
GHI	Global Horizontal Irradiance	PV/T	Photovoltaic/Thermal
GME	Gestore dei Mercati Energetici	RED	Reverse Electrodialysis
IEA	International Energy Agency	RES	Renewable Energy Sources
IRR	Internal Rate of Return	RO	Reverse Osmosis
LC	Levelized Cost	SAPM	Sandia Array Performance Model
LCA	Life Cycle Assessment	SBX	Simulated Binary Crossover
LCOMg	Levelized Cost of Magnesium Hydroxide production	SOC	State of Charge
LHS	Latin Hypercube Sampling	SSP	Scambio Sul Posto
MD	Membrane Distillation	TMY	Typical Meteorological Year
MGP	Mercato del Giorno Prima,	TRL	Technology Readiness Level
MSMD	Multistage Membrane Distillation		

and Haralambous [6] review minimal- and zero-liquid-discharge strategies as alternatives that avoid such impacts while enabling resource recovery from the concentrated stream. Sewer disposal remains a low-cost option for small-scale facilities, yet elevated salinity and chemical loads can inhibit biological processes in wastewater treatment plants and accelerate infrastructure corrosion, prompting utilities to restrict or prohibit such discharges [7].

Given the limitations of conventional disposal methods, current research and industrial development increasingly promote brine management solutions aligned with circular-economy principles, aiming at maximising water recovery and enabling as the extraction of elements such as magnesium, potassium, lithium, and boron, from desalination brines [8]. Many of these are listed as critical raw materials (CRM) due to their poor availability in Europe and to high-risk, geopolitically sensitive supply chains [9]. In this framework, the concept of circular desalination has emerged, where brine is no longer treated solely as a waste stream but as a secondary resource. Integrated treatment chains are being proposed and tested at pilot scale, such as the WATER-MINING Mild Liquid Discharge (MLD) scheme in Lampedusa [10], and the SEArcularMINE process, which targets the full valorisation of saltworks bitterns – the highly concentrated residual brines left by progressive evaporation and crystallisation in table-salt production, sometimes up to twenty times more saline than seawater – through magnesium recovery, internal reagent production and selective extraction of trace elements. Recent outputs include a pilot-scale crystallizer for high-purity $Mg(OH)_2$ from real saltworks bitterns [11], and an ultrafiltration pilot unit for ultra-concentrated brines as part of an integrated chain [12], confirming the technical feasibility of circular brine valorisation under real operating conditions.

Among emerging circular treatment schemes, one particularly promising configuration is the chain developed within the CARMEn (A novel *C*ircular *A*pproach to *R*ecover Critical Raw *M*aterials and *En*ergy from Spent Seawater Brines) project [13], designed to valorize saline solutions such as reverse osmosis (RO) brines and saltworks bitterns. RO brines can be directed either to a crystallizer for magnesium recovery as $Mg(OH)_2$, or to a nanofiltration (NF) unit for bivalent ion enrichment before $Mg(OH)_2$ extraction. In the case of bitterns, due to their very high salinity, the NF stage cannot be applied, thus bitterns are solely treated in $Mg(OH)_2$ crystallizers. After solids separation, the clarified stream is softened and fed to electrodialysis with bipolar membranes (EDBM) unit, which generates soda and acid used internally by the reactor and the softening resin. The residual saline solution is subsequently concentrated in a membrane distillation (MD) unit to produce high-purity freshwater. The remaining concentrated brine is valorised in a reverse electrodialysis (RED) system exploiting the concentration gradient between the concentrated brine and reclaimed water to produce electrical energy, while the final effluent, with composition comparable to seawater, can be safely discharged, closing the loop..

Despite its strong process performance, the CARMEn chain is energy intensive from both the electrical and thermal perspectives. The EDBM unit imposes a continuous electrical load, while the MD unit requires a stable thermal input at relatively low temperatures (50–80 °C). Moreover, MD is still a relatively low-technology readiness level (TRL) desalination technology and its energy efficiency is not yet fully optimised. For these reasons, the integration of renewable energy sources (RES) is crucial to render such treatment chains environmentally and economically sustainable.

In recent years, an increasing number of studies have investigated the coupling of EDBM with photovoltaic (PV) generation, mostly at lab scale (TRL $\approx$ 4), demonstrating that PV-EDBM can achieve techno-economic performance comparable to grid-powered operation [14]. Herrero-Gonzalez et al. [15] showed that a lab-scale EDBM unit powered by a 1.125 m^2 PV panel achieved a 40 % reduction in specific energy consumption for HCl production, while Cassaro et al. [16] reported extended pilot-scale campaigns where EDBM operated continuously in summer and winter using renewable energy, confirming the robustness of EDBM–RES coupling at higher TRL.

In parallel, membrane distillation has been extensively explored in combination with solar energy systems to produce freshwater while recovering thermal and, in some configurations, electrical energy. Two main strategies dominate: (i) using PV waste heat to drive MD processes and (ii) employing photovoltaic/thermal (PV/T) or concentrated photovoltaic (CPV) units to supply both heat and power. Wang et al. [17] proposed a multistage PV–MD (MSMD) system, in where which a cascaded MD module mounted behind a PV panel simultaneously generates electricity (>11 % PV efficiency thanks to cooling) and freshwater (~1.7 $kg \cdot m^{-2} \cdot h^{-1}$). Building on this concept, Amiruddin et al. [18] developed a multilayered –photovoltaic/air–gap MD (AGMD) system for ultrapure water production, later optimized by Fang et al. [19] through system-level design refinements. At higher solar concentration, Rabie et al. [20] investigated a hybrid CPV–DCMD unit where CPV cooling heat drives desalination, achieving compact designs with improved energy efficiency and water yield. At pilot scale, Bouguecha et al. [21] demonstrated a solar-powered DCMD plant combining flat-plate collectors and PV panels with a 3.39 m^2 membrane area, reporting a 31.3 % improvement in solar-thermal efficiency through heat recovery. Several studies have also coupled MD with low-grade waste heat (35–80 °C) from district heating, CHP plants and industrial cooling circuits, using indirect configurations with heat exchangers and thermal storage to buffer intermittency and stabilise permeate flux [22].

Although the application of EDBM and MD powered by renewable energy sources has been demonstrated at both lab and pilot scales, no previous study has integrated both units within a single circular desalination treatment chain and simultaneously co-designed the renewable-energy system that powers them. In each of the MD-focused studies above, single membrane unit is considered in isolation, without battery storage, thermal storage, or integration into a multi-stage process chain. The literature does not yet offer multi-objective co-optimisation frameworks that jointly size PV systems, battery storage, solar-thermal collectors and thermal storage to meet the time-varying electrical and thermal demands of an integrated (CARMEn-type) process under realistic solar resource profiles, electricity tariffs, grid export remuneration schemes and evolving regulatory incentive frameworks.

The novelty of the present framework therefore lies not in the individual modelling or optimization techniques employed – photovoltaic performance modelling via pvlib, rule-based energy dispatch, discounted cash-flow analysis and evolutionary multi-objective optimization are all established methods – but in their integration into a substantially more complex co-design problem than is typically addressed in the literature. Specifically: (i) to the authors' knowledge, this is the first framework to jointly size four coupled subsystems (PV, battery, solar-thermal collectors and thermal storage) against simultaneous, explicit electrical and thermal self-sufficiency objectives for an integrated, multi-stage circular brine-valorisation chain, rather than the one- or two-variable PV-battery or PV-thermal sizing problems common in prior studies; (ii) the battery decision space is itself scenario-adaptive, with its minimum bound derived from process-specific resilience requirements rather than fixed a priori; (iii) the dispatch logic couples electrical and thermal storage management under a shared resilience-first philosophy, with a conditional economic-export override tied to real regulatory remuneration mechanisms; and (iv) each candidate design is evaluated through a full 8760-hour hourly dispatch simulation nested inside the evolutionary optimisation loop, coupling techno-economic, environmental and reliability performance within a single four-objective Pareto search. Beyond the framework itself, the resulting scenario-specific findings including an economic break-even threshold for battery investment and the quantification of the achievable reduction in the levelized cost of Magnesium Hydroxide production (LCOMg) provide transferable, practice-relevant design guidance not previously available for this class of circular desalination system.

The multi-objective nature of the co-design problem – simultaneously targeting economic profitability, energy self-sufficiency, carbon mitigation and system reliability – requires an optimisation strategy capable of exploring complex Pareto fronts in a multi-dimensional, non-linear decision space. For this reason, Non-dominated Sorting Genetic Algorithm II (NSGA-II) was adopted, being a well-established evolutionary algorithm widely used for sizing hybrid renewable energy systems. Prior work has demonstrated its suitability for optimising PV–battery configurations under multiple conflicting objectives [23], for hybrid PV–wind–storage systems where renewable intermittency and storage constraints must be managed [24], and for yielding well-distributed Pareto fronts in complex techno-economic optimisation of distributed energy systems [25]. Collectively, these studies confirm that NSGA-II effectively handles conflicting objectives, non-convex solution spaces and mixed discrete–continuous design variables. These properties are particularly relevant to the present co-design problem, which involves four simultaneous objectives (net present value, electrical coverage, thermal coverage and capital expenditure – CAPEX), scenario-dependent adaptive constraints, and a dispatch logic whose non-linear interactions between PV sizing, battery operation and grid export make gradient-based methods unsuitable.

This study addresses these gaps for the CARMEn brine-valorisation chain coupled with a hybrid solar energy supply. Three industrially representative feed scenarios are analyzed – saltworks bittern, NF retentate and RO brine – covering a wide range of Mg^{2+} concentrations, from 2.45 g/L in RO brine as reported for the CARMEn chain [13] to 49 g/L typical of saltworks bitterns documented in the broader brine-valorisation literature [26]. Thermal and electrical loads are taken from the techno-economic study of Scelfo et al. [27] at operating pH values of 10.6, 10.6 and 12, respectively. For each scenario, the framework quantifies key performance indicators including the PV self-consumption ratio, the fraction of electrical and thermal energy demands covered by on-site renewables, battery cycling behavior, CO_2 emissions avoided, and financial metrics such as Net Present Value (NPV), Internal Rate of Return (IRR), and discounted payback period. Results are obtained for a single Mediterranean site (Trapani, Italy), a single Typical Meteorological Year dataset, and three fixed process operating conditions. While the co-design methodology itself – joint sizing of PV, battery, solar-thermal and thermal-storage capacity against coupled electrical and thermal demand – is readily transferable to other sites and processes, its quantitative conclusions (optimal sizing, economic viability thresholds, achievable renewable coverage) are specific to this climatic and regulatory context and should be re-evaluated, rather than extrapolated, for sites with materially different solar resource, energy market structure, or process characteristics.

2. Materials and Methods

This section presents the integrated modelling and optimisation framework developed to evaluate hybrid renewable energy systems for the CARMEn brine valorisation chain. Section 2.1 describes the CARMEn treatment chain and the structure of the coupled renewable energy supply. Section 2.2 introduces the overall simulation architecture, followed by detailed descriptions of the photovoltaic, battery, thermal, economic and environmental sub-models (Sections 2.3-2.7), the multi-objective optimisation formulation (Section 2.8), the performance indicators (Section 2.9), and the sensitivity and uncertainty analysis protocol (Section 2.10).

2.1. Integrated system: CARMEn treatment chain and hybrid renewable energy supply

In this work, the CARMEn treatment chain [13] is integrated with a hybrid renewable energy system designed to supply both electrical and thermal demands of the process, as schematically illustrated in Fig. 1. The renewable section consists of a PV field coupled with a lithium-ion battery storage system for the electrical subsystem, and a solar-thermal field composed of flat-plate collectors combined with a hot-water storage tank for the thermal subsystem. The electrical energy produced by the PV system is used to supply the main process units, primarily the electrodialysis with bipolar membranes system and, when present, the nanofiltration unit, which together represent the dominant electrical loads of the chain. The battery system provides short-term energy storage, enabling temporal decoupling between PV generation and process demand. On the thermal side, the heat required by the membrane distillation unit is supplied by the solar-thermal collectors, with the thermal storage tank ensuring stable operation by buffering intraday fluctuations in solar availability.

Two alternative operating configurations are considered in this study: grid-connected and fully renewable (stand-alone). In the grid-connected configuration, the PV system acts as the primary energy source, and the generated electricity can be directly used to supply the process, stored in the battery, or exported to the grid. In the fully renewable configuration, the system operates without grid support, and all electrical demand must be met by PV generation and battery storage, with any residual unmet demand accounted for as unserved energy, which directly penalises the coverage objective in the optimisation. For the thermal subsystem, solar collectors and thermal storage remain the

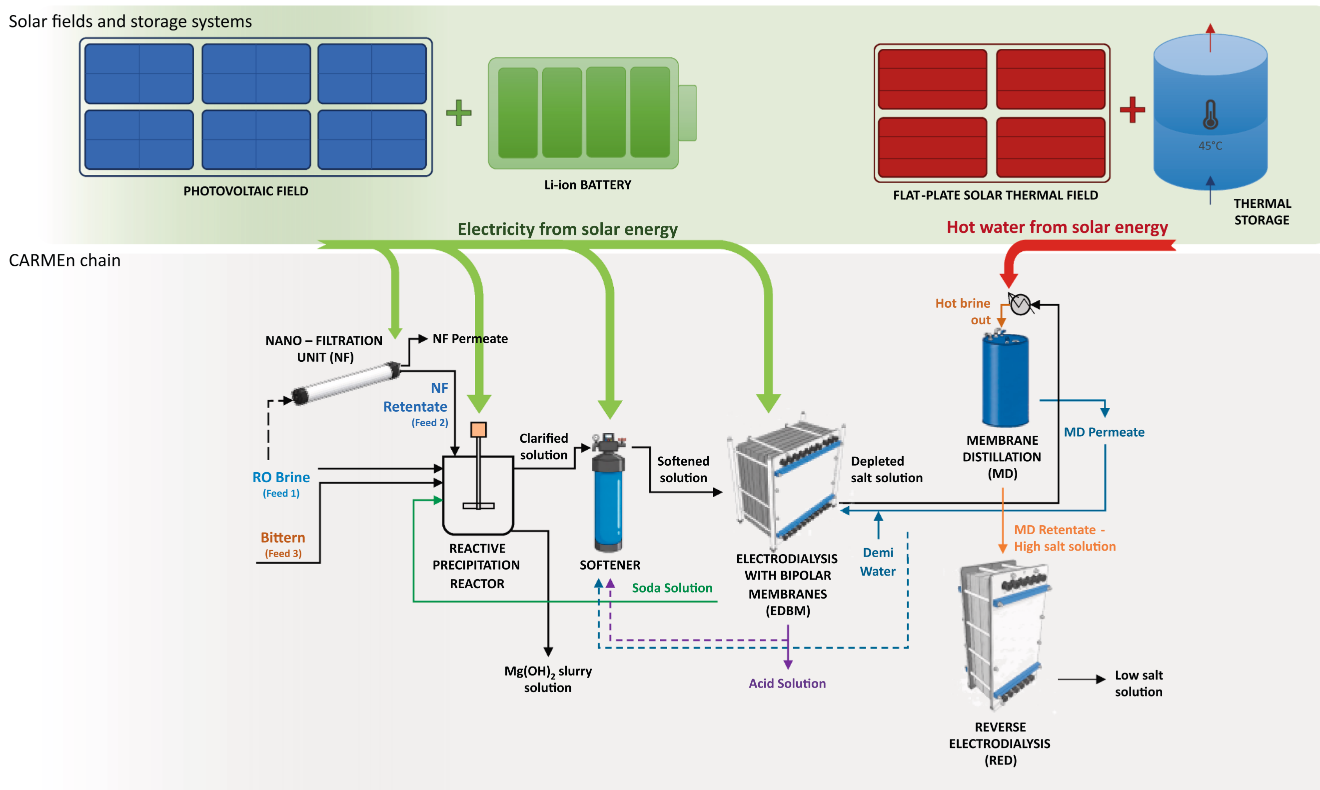

Fig. 1. Schematic representation of the CARMEn treatment chain integrated with the hybrid renewable energy system, including electrical and thermal subsystems.

primary sources in both configurations, while an auxiliary gas boiler provides backup when renewable heat supply is insufficient. The dispatch logic governing these interactions is presented in Section 2.4.

2.2. Modelling framework overview

A dynamic techno-economic simulation framework was developed in Python to evaluate and optimise the hybrid renewable-energy integration of the CARMEn treatment chain across three industrial scenarios (RO brine, NF retentate, and saltwork bittern) under both grid-connected and fully renewable (stand-alone) configurations. The modelling architecture follows a modular structure in which each physical or economic subsystem (photovoltaic generation, battery dispatch, solar-thermal production, thermal storage, and economic-environmental accounting) is implemented as an independent Python function. All components are coordinated by the main simulation routine (*simulate_system_system()*), which ensures consistent hourly mass-energy balances over a full meteorological year (8760 h). Fig. 2 summarises the structure of the modelling and optimisation framework, highlighting the sequential progression from input data ingestion to annual co-simulation, multi-objective optimisation and final post-processing stages. The complete code is publicly available in the Zenodo repository associated with this study (see *Data availability*).

2.3. Photovoltaic system model

The PV subsystem was modelled using a physics-based approach implemented in Python in the function *simulate_pv_production()* by using the open-source library *pvlib* [28], which provides validated reference implementations for the simulation of solar energy systems. The *ModelChain* architecture of *pvlib* allows combining multiple sub-models (solar geometry, irradiance transposition, cell temperature, and DC/AC conversion) into a single reproducible workflow. This modular structure ensures a balance between physical accuracy and computational efficiency, essential in the multi-objective optimisation framework adopted in this study.

Hourly simulations were performed using Typical Meteorological Year () data extracted from the Photovoltaic Geographical Information System (PVGIS) database [29], accessed programmatically through the pvlib iotools interface [30]. The meteorological inputs include global, direct normal, and diffuse horizontal irradiance (GHI, DNI, DHI), ambient temperature, and wind speed. Solar zenith and azimuth angles were computed as a function of time, date, and site coordinates, and all data were harmonized to the Europe/Rome time zone. Hourly time series with 8760 records were obtained to represent an annual profile.

Since PVGIS TMY datasets do not provide plane-of-array (POA) irradiance, the total in-plane irradiance (G_{POA}) was reconstructed from GHI, DNI, and DHI components through the Hay-Davies transposition model (see Equation (1)), implemented internally in the function *simulate_pv_production()*. This anisotropic sky model was originally formulated by Hay and Davies [31] and subsequently refined by Perez et al. [32], who introduced a new simplified version of the diffuse irradiance model for tilted surfaces, and later extended by Perez et al. [33] to account for circumsolar and horizon brightening effects. Loutzenhiser et al. [33] empirically validated these anisotropic approaches against measured data for building energy simulation, reporting a 3–5% annual accuracy improvement over the isotropic approach under clear-sky conditions consistent with the Mediterranean climate considered here. The total irradiance incident on the tilted PV array is given by:

$$G_{POA} = G_b \cdot \cos\vartheta_i + G_{d,\,Hay-Davies} + G_r \tag{1}$$

where G_b is the beam component on the module plane (W·m^{-2}), ϑ_i is the solar incidence angle, $G_{d,\,Hay-Davies}$ is the diffuse component from the Hay-Davies model (W·m^{-2}), and G_r is the ground-reflected irradiance (W·m^{-2}), computed assuming constant albedo of 0.20.

The module operating temperature (T_m) is evaluated with the Sandia Array Performance Model (SAPM) [34], using three empirically-determined coefficients a, b, and ΔT:

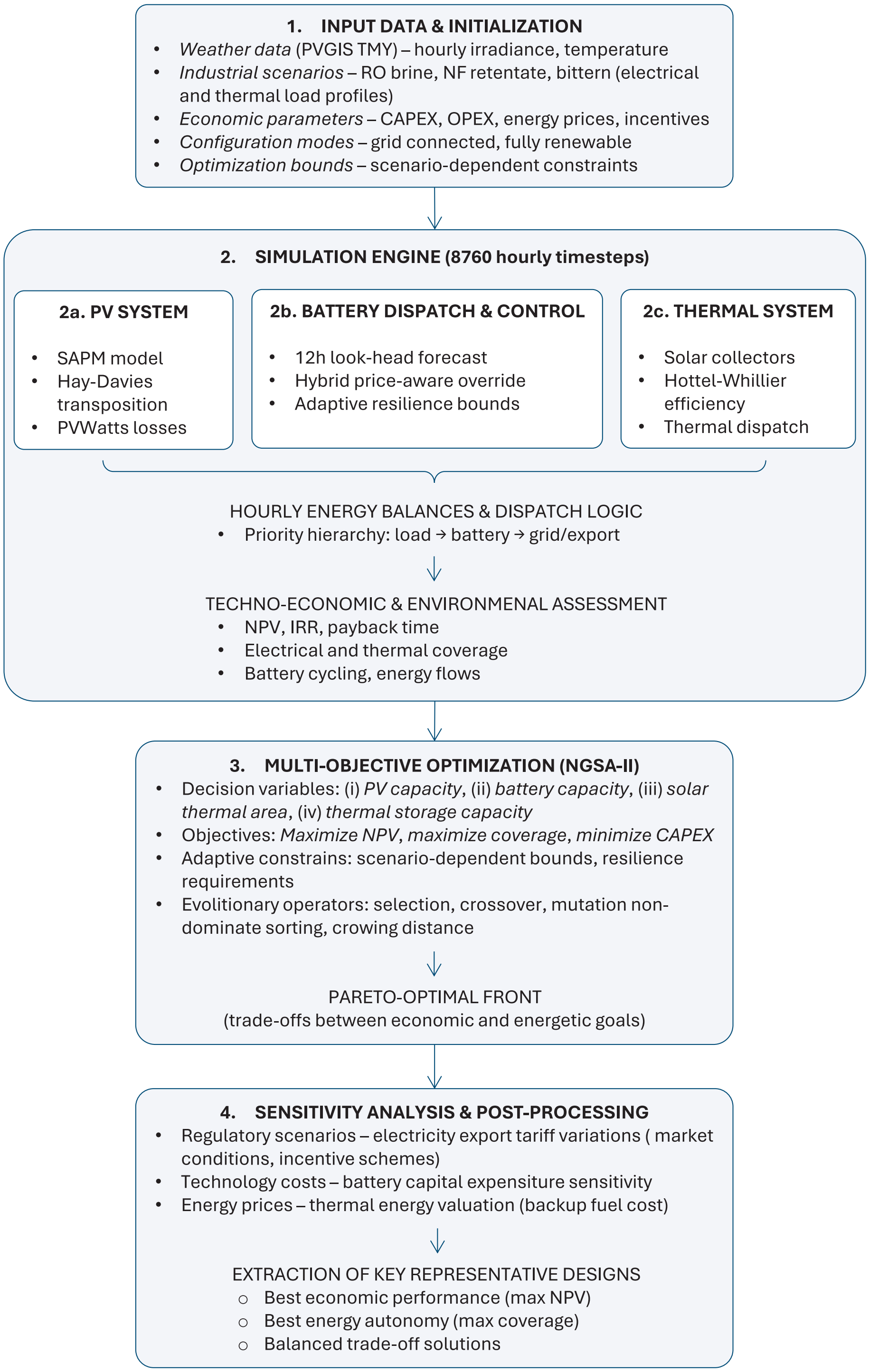

Fig. 2. Overview of the integrated modelling and optimisation framework. The diagram summarises the four main modules: (1) input data and initialisation, (2) annual simulation of renewable supply, energy dispatch and techno-economic–environmental assessment, (3) multi-objective NSGA-II optimisation, and (4) sensitivity analysis and post-processing.

$$T_m = T_a + G_{POA} \cdot \exp(a + b \cdot v_w) + \frac{G_{POA}}{1000} \cdot \Delta T \tag{2}$$

where, T_a is the ambient temperature (°C), v_w is the wind speed (m·s^{-1}), a accounts for convective heat losses at near-stagnant air conditions, b represents the influence of wind on the thermal losses, and ΔT is the reference temperature difference between the cell and the module back surface at 1000 W·m^{-2}. For an "open-rack, glass-glass" mounting configuration, the adopted coefficients ($a = -3.47$, $b = -0.0594$, and $\Delta T = 3$°C) were taken from Sandia Array Performance Model empirical coefficient tables [34], with their applicability further supported by the wind-speed sensitivity analysis of Anderson et al. [35]. Then, the cell temperature is internally derived from the module temperature as:

$$T_{cell} = T_m + \frac{G_{POA}}{1000} \cdot \Delta T \tag{3}$$

The DC electrical output is computed following the *PVWatts* formulation [36], which relates power to irradiance and cell temperature as:

$$P_{DC} = P_{DC,0} \cdot \frac{G_{POA}}{1000} \cdot [1 + \gamma \cdot (T_{cell} - 25)] \tag{4}$$

where $P_{DC,0}$ is the nominal DC power (W) at reference conditions (1000 W·m^{-2} and 25°C), and γ is the temperature coefficient (= -0.004°C^{-1}). The AC power is obtained using the *PVWatts* inverter model with a constant efficiency ($\eta_{inv} = 96\%$), and aggregate system losses (ohmic, mismatch, wiring, soiling, etc.) are represented by a single loss factor $L = 0.14$[37]. The resulting net hourly AC power profile is expressed as:

$$P_{AC,\,net} = \eta_{inv} \cdot (1 - L) \cdot P_{DC} \tag{5}$$

The hourly AC power series $(P_{AC,\,net})$ is then used consistently in the energy dispatch, economics and environmental accounting modules. A yearly PV degradation rate of 0.8%, that is applied exclusively in the discounted-cash-flow model, accounts for the gradual decline of module electrical performance caused by encapsulant ageing, UV exposure, corrosion, and increased series resistance. This value aligns with the degradation-rate ranges reported in the analytical review by Jordan and Kurtz [38] and updated in their subsequent compendium of field degradation data [39].

2.4. Battery dispatch strategy and hybrid economic control

The battery energy storage system is simulated through an hourly rule-based dispatch algorithm that integrates physical constraints (charging/discharging efficiencies and state-of-charge (SOC) bounds) with anticipatory look-ahead control and, in grid-connected configurations, a price-aware surplus export mechanism. The dispatch logic is implemented in the function *simulate_energy_system()* and operates on an hourly energy basis (kWh per timestep), ensuring strict energy balance at each step.

At each timestamp, the instantaneous power balance between photovoltaic generation $(P_{PV}(t))$ and electrical load $(P_L(t))$ defines the net surplus of deficit:

$$S(t) = P_{PV}(t) - P_L(t) \tag{6}$$

PV generation is always allocated to the process load with absolute priority: $E_{PV \to L}(t) = \min(P_{PV}(t), P_L(t))$.

To enhance operational resilience and reduce unnecessary cycling, a 12-hour look-ahead window derived from TMY data is implemented. Since the TMY is fully known in advance, the look-ahead is deterministic, involving no forecasting uncertainty (the future PV and load arrays are pre-computed once before the main dispatch loop); the implications of this perfect-foresight idealisation are discussed in Section 4.5. For each timestep, cumulative future PV generation (PV_{fut}) and electrical demand (L_{fut}) over the horizon $H = 12$ h are computed as in Equations (7)-(8).

$$PV_{fut}(t) = \sum_{k=1}^{H} P_{PV}(t+k) \tag{7}$$

$$L_{fut}(t) = \sum_{k=1}^{H} P_L(t+k) \tag{8}$$

The anticipated net deficit over the look-ahead horizon $(D_{fut}(t))$ is then used to define a dynamic minimum SOC target $(E_{target}(t))$ (expressed in energy units, kWh) that the battery must preserve:

$$D_{fut}(t) = \max\left(0, L_{fut}(t) - PV_{fut}(t)\right) \tag{9}$$

$$E_{target}(t) = \max\left(E_{res}, \min\left(\frac{D_{fut}(t)}{\eta_{dis}}, E_{\max}\right)\right) \tag{10}$$

This target is bounded between a fixed resilience reserve $E_{res} = SOC_{reserve} \cdot C_{batt}$ - where $SOC_{reserve} = 0.20$ is the minimum state-of charge fraction retained for instantaneous blackout events, and C_{bat} is the nominal battery energy capacity - and the upper bound $E_{\max} = SOC_{\max} \cdot C_{batt}$, where $SOC_{\max} = 0.90$ is the maximum allowable state of charge. It is important to note that $SOC_{reserve}$ is distinct from the hard lower bound of the state of charge of the battery ($SOC_{\min} = 0.10$), below which battery operation is never permitted.

During deficit periods ($S(t) < 0$), battery discharge is allowed only when the stored energy exceeds the dynamic target (Equation (11):

$$E_{bat \to L}(t) = \min\left(\left(E_{SOC}(t) - E_{target}(t)\right) \cdot \eta_{dis}, -S(t)\right) \tag{11}$$

where, $E_{SOC}(t) = SOC(t) \cdot C_{batt}$ is the instantaneous stored energy, in the battery at time t, $E_{target}(t)$ is the dynamic minimum SOC target defined in Equation (9), η_{dis} is the battery discharging efficiency, and $S(t)$ is the net power surplus or deficit at time t. The dischargeable energy is limited as in Equation (11). If the SOC is at or below the target, stored energy is preserved and the discharge is inhibited; the remaining deficit is covered by grid import in grid-connected configurations or classified as unserved load in fully renewable systems. An optional weekly cell-balancing routine forces discharge to the minimum SOC at fixed intervals of 168 hours (once per week), emulating period capacity verification. This routine is active only in grid-connected mode.

During surplus periods ($S(t) \geqslant 0$), PV surplus is directed to battery charging up to the available SOC headroom, defined as the energy that can still be stored before reaching the upper bound $E_{\max} = SOC_{\max} \cdot C_{batt}$. The charge energy allocated at each timestep is given by Equations 12-13:

$$E_{room}(t) = E_{\max} - E_{SOC}(t) \tag{12}$$

$$E_{PV \to bat}(t) = \min\left(S(t), \frac{E_{room}(t)}{\eta_{ch}}\right) \tag{13}$$

where, $E_{room}(t)$ is the available SOC headroom at time t, and $E_{SOC}(t)$ is the instantaneous stored energy. In Equation (13), $E_{PV \to batt}(t)$ is the energy directed from PV to battery charging at timestep t, and η_{ch} is the battery charging efficiency.

In grid-connected configurations, a hybrid price-aware override is evaluated at each surplus timestep. When the hourly grid export remuneration $p_{SSP}(t)$(the *Scambio Sul Posto* SSP mechanism is regulated under Italian energy policy frameworks [40]) exceeds the retail import price c_{grid}:

$$p_{SSP}(t) > c_{grid} \tag{14}$$

the override activates and the entire PV surplus is exported directly to the grid rather than stored. This condition reflects scenarios where export incentives, such as the Italian *Comunità Energetiche Rinnovabili (CER* - Renewable Energy Community*)* scheme [41], make immediate export economically preferable to storage and subsequent self-consumption. Under baseline market conditions ($p_{SSP} \approx 0.108$ €/kWh $< c_{grid} = 0.22$ €/kWh), the condition in Equation (14) is never satisfied and the override remain inactive, yielding dispatch behaviour identical to the resilience-only logic. The override activates exclusively when partial or fully CER incentive levels are considered.

Charging and discharging efficiencies were set to $\eta_{ch} = \eta_{dis} = 0.95$, consistent with the 85–90% -round-trip efficiency reported for lithium-ion systems in utility-scale battery storage cost projections [42] and in techno-economic assessments of PV-storage systems [43]. SOC dynamics follow the discrete hourly balance that updates it considering charging and discharging energy flows at each time step:

$$E_{SOC}(t) = E_{SOC}(t-1) + \eta_{ch} \cdot E_{PV \to batt}(t) - \frac{E_{batt \to L}(t)}{\eta_{dis}} \tag{15}$$

where $E_{PV \to batt}(t)$ and $E_{batt \to L}(t)$ [kWh] are the hourly charge (PV to battery) and discharge energies (battery to load), before and after efficiency losses. SOC is constrained within the admissible operating window $[SOC_{\min}, SOC_{\max}] = [0.10, 0.90]$, in line with the storage-performance measurement protocol of Ferreira et al. [44] and the operational assumptions adopted in the REopt techno-economic model [45].

Battery cycling intensity is quantified as equivalent full cycles per year:

$$N_{cycles} = \frac{\sum_t E_{batt\rightarrow L}(t)}{\eta_{dis} \cdot C_{batt}} \tag{16}$$

This metric is used exclusively within the economic degradation module and does not influence dispatch decisions. The complete dispatch structure, including dynamic SOC targeting and hybrid economic override, is illustrated as a flowchart in *Supplementary Fig. S1*.

2.5. Thermal energy subsystem model

The thermal subsystem consists of a field of flat-plate solar collectors coupled with a hot water storage tank, designed to supply the heat requirements of the MD unit. The MD module operates with a feed temperature of approximately 45°C and requires a continuous thermal input to maintain this temperature. In the simulations, this heat demand was assumed as a constant load profile to reflect a steady MD operation. Any thermal demand not met by the solar system is assumed to be provided by a backup source (e.g. a gas boiler), ensuring the MD process can always run at the required temperature. Conversely, any surplus solar heat beyond the instantaneous MD needs can be stored or is otherwise curtailed.

The solar-thermal collector field and the hot-water storage tank are modeled through the functions *simulate_solar_thermal()* and *simulate_energy_system()*.

2.5.1. Solar collector efficiency model

The useful heat output of the solar collectors was computed using a simplified form of the Hottel-Whillier-Bliss equation for flat-plate collectors [46]. At each hour t, the thermal power solar-generated is given by:

$$P_{th}(t) = A_{coll} \cdot G_{POA}(t) \cdot \eta_{coll}(t) \tag{17}$$

where A_{coll} is the total collector area (decision variable in the optimisation algorithm), $G_{POA}(t)$ is the in-plane solar irradiance on the collector surface [W·m^{-2}], and $\eta_{coll}(t)$ is the instantaneous collector efficiency. The plane-of-array irradiance values were derived using the Hay-Davies transposition model, in accordance with the methodology adopted for the PV subsystem, ensuring uniform solar resource inputs across technologies. The collector efficiency is estimated using a linearized Hottel-Whillier-Bliss formulation:

$$\eta_{coll}(t) = \eta_0 - a_1 \cdot \frac{T_{mean}(t) - T_a(t)}{G_{POA}(t)} \tag{18}$$

where η_0 represents the optical efficiency of the collector at reference conditions, a_1 is the first-order heat loss coefficient [W/(m^2·K)], $T_{mean}(t)$ is the mean fluid temperature in the collector [°C], and $T_a(t)$ is the ambient air temperature [°C] [46]. The collector efficiency is η_{coll} is constrained between 0 and 0.85 to reflect practical operating limits, and is set to zero when $G_{POA} < 50\ W/m^2$. The collector efficiency (Equation (18) is evaluated at a constant mean fluid temperature T_{mean}= 32.5°C, taken as the arithmetic mean of the process inlet and outlet temperatures of 45°C and 20°C. This value is held constant throughout the simulation and does not vary with thermal-storage state of charge or MD operating conditions. The adopted parameter values are reported in *Section S2.2* of *Supplementary Material*.

2.5.2. Thermal storage and dispatch

To maximize solar heat utilisation, a hot-water thermal storage unit is included, whose energy capacity $(E_{th,store})$ is treated as a decision variable in the optimisation. The storage is modelled as an insulated sensible storage tank with an overall round-trip efficiency $\eta_{rt} = 0.85$, consistent with the typical performance range (0.8 – 0.9) of well-insulated hot-water systems [47]. A standing loss rate of 2% per day is applied, in line with experimental observations for large-scale water tanks [47].

The dispatch logic priorities direct use of solar heat for the MD load, using the tank to buffer surpluses and deficits. When solar output exceeds the instantaneous MD demand, the excess is diverted to charge the storage up to its capacity, with the charging efficiency penalty applied; any unused heat is curtailed. When solar output is insufficient, the storage discharges to cover the shortfall, subject to the available state of charge and discharge efficiency. Any residual deficit is supplied by the auxiliary gas boiler in grid-connected configurations or accounted for as unserved thermal energy in fully renewable mode.

The state of charge of the thermal tank is tracked over time considering charge-discharge flows and standing losses, applied at each hourly timestep prior to dispatch. The storage is initialised as empty at the start of the simulation (worst-case assumption). This integrated thermal model enables the calculation of a thermal self-sufficiency metric (C_{th}) analogous to the electric case – i.e. the fraction of the MD heat demand supplied by the solar collectors either directly or via storage – as defined in Section 2.9.

2.6. Economic model

The economic model performs a deterministic techno-financial evaluation of each candidate configuration generated by the optimisation framework. It quantifies investment costs, annual operating expenses, energy-rated savings, and carbon-credit revenues within a unified discounted-cash-flow formulation, providing the Net Present Value and other derived economic indicators [48]. The model is implemented within the function *simulate_energy_system()*.

For each configuration, the total capital expenditure (C_{tot}) is computed as the sum of the investments associated with the photovoltaic field, the battery storage system, the solar thermal collectors, the thermal storage tank, and the auxiliary gas boiler:

$$C_{tot} = c_{PV} \cdot P_{PV} + c_{batt} \cdot C_{batt} + c_{coll} \cdot A_{coll} + c_{th,\ store} \cdot E_{th,\ store} + c_{boiler} \cdot P_{th,\ peak} \tag{19}$$

where P_{PV} [kW$_p$], C_{batt} [kWh], A_{coll} [m^2], and $E_{th,\ store}$ [kWh] are the decision variables representing the installed capacities, and c_i are the corresponding unit investment costs. The auxiliary gas boiler is sized at the peak thermal load $(P_{th,\ peak})$ [kW$_{th}$], with the unit cost c_{boiler}. Since thermal loads are modelled as flat profiles, $P_{th,\ peak}$ coincides with the nominal thermal demand of each scenario. The boiler is replaced once during the project lifetime (at year 15), with the replacement cost discounted to present value. Note that C_{tot} corresponds to the CAPEX objective in the optimisation framework (Section 2.8), where it appears as $-C_{tot}$ to allow minimisation within a maximisation problem.

Hourly energy simulations are aggregated into annual balances to determine electrical and thermal energy flows. The yearly economic benefit (B_y) at year y is expressed as:

$$B_y = \left(E_{self,y} \cdot c_{grid} - E_{imp,y} \cdot c_{grid} + E_{\exp,y} \cdot p_{SSP,y}\right) + Q_{sol,y} \cdot c_{th} + C_{CO_2,y} \tag{20}$$

where $E_{self,y}$ is the annual electrical energy served on site (by PV and battery), representing the baseline grid cost avoided; $E_{imp,y}$ is the residual annual grid import; $E_{\exp,y}$ is the annual exported energy, $Q_{sol,y}$ is the useful thermal energy delivered by the solar subsystem (directly and via storage);c_{grid} is the retail electricity import tariff; $p_{SSP,y}$ is the annual-average export remuneration under the *Scambio Sul Posto* mechanism; c_{th} is the reference thermal energy cost representing the unit cost of heat that would otherwise be supplied by the gas boiler; and $C_{CO_2,y}$ is the monetized carbon benefit as detailed in *Section 2.7*. The annual boiler gas cost, corresponding to the thermal energy not covered by the solar subsystem, is treated as a fuel operating cost and subtracted separately within the cash-flow structure. Annual operation and maintenance costs are modelled as fixed fractions of the respective CAPEX components, as reported in , and remain constant in real terms over the system lifetime. Component degradation is accounted for by an annual derating factor applied to PV-derived energy benefits $\varphi_y = (1-\delta_{PV})^{y-1}$, where $\delta_{PV} = 0.8\%/y$ is the PV degradation rate defined in . The Net Present Value of each configuration is then computed as:

$$NPV = -C_{tot} + \sum_{y=1}^{N} \frac{(B_y - OM_y - C_{gas,y} - R_y)}{(1+r)^y} \tag{21}$$

where r is the real discounted rate and N the project lifetime in years, both reported in ; OM_y is the annual operation and maintenance cost, computed as fixed fractions of the respective CAPEX components () and assumed constant over the project lifetime; $C_{gas,y}$ is the annual gas boiler fuel cost, evaluated as $C_{gas,y} = Q_{boiler,y} \cdot c_{th,ref}$, where $Q_{boiler,y}$ is the thermal energy not covered by the solar subsystem at year y; and R_y is the replacement cost of battery or thermal storage components at the years specified in , zero otherwise.

The Internal Rate of Return (*IRR*) is obtained as the rate r^* that satisfies:

$$0 = -C_{tot} + \sum_{y=1}^{N} \frac{(B_y - OM_y - C_{gas,y} - R_y)}{(1+r)^y} \tag{22}$$

and the discounted payback time (*DPBT*) is defined as:

$$DPBT = \min\left\{ y \in \mathbb{N} : \sum_{k=1}^{y} \frac{(B_k - OM_k - C_{gas,k} - R_k)}{(1+r)^k} \geqslant C_{tot} \right\} \tag{23}$$

The IRR computation is performed numerically using the *numpy-financial* Python package[49], consistent with standard financial-computation practices in Python [50]. All economic quantities are expressed at constant price levels in the baseline configuration; *Section 2.10* relaxes this assumption for the export tariff and thermal energy through dedicated sensitivity and uncertainty analyses.

2.7. Environmental model

The environmental model quantifies the avoided carbon dioxide (CO_2) emissions associated with the renewable energy contribution of each system configuration. It evaluates both the electrical and thermal shares of the displaced conventional energy sources, converting them into equivalent avoided emissions and integrating their monetary value directly into the cash-flow structure of the economic model (as described in *Section 2.6*). The total avoided emissions for each year y are computed as:

$$M_{CO_2,y} = E_{self,y} \cdot EF_{el} + Q_{sol,y} \cdot EF_{th} \tag{24}$$

where $E_{self,y}$ [kWh] is the annual self-consumed electrical energy, $Q_{sol,y}$ [kWh_{th}] is the useful thermal energy delivered by the solar field, and EF_{el} and EF_{th} [$kgCO_2$/kWh] are the emission factors associated with the national electrical grid and an efficient natural gas-boiler, respectively [51]. The first term accounts for avoided grid-related emissions through renewable self-consumption, while the second term represents avoided thermal emissions due to solar heat production. Exported PV electricity is deliberately excluded from carbon accounting, consistently with a conservative approach that attributes emission credits only to directly displaced energy consumption.

The annual avoided emissions $(M_{CO_2,y})$ [$kgCO_2$/y] are then converted into tonnes of CO_2 and monetised through a constant carbon price p_{CO_2} [€/tCO_2]:

$$C_{CO_2,y} = \frac{M_{CO_2,y}}{1000} \cdot p_{CO_2} \tag{25}$$

This value is incorporated directly into the annual economic benefit (B_y) of the discounted-cash-flow formulation (Equation (20), ensuring that environmental and economic performance are jointly evaluated. All emission factors and the carbon price are treated as scenario-dependent parameters and are defined explicitly in *Section S2.5* of *Supplementary Material*.

The environmental assessment above is limited to operational emissions avoided through renewable self-consumption; it does not include embodied (upstream, manufacturing-stage) emissions associated with the renewable components themselves. To gauge the materiality of this scope limitation, a screening-level embodied-emissions estimate was performed for the PV modules, battery, solar-thermal collectors and thermal storage tank of each optimised configuration, using representative emission factors from the life-cycle assessment literature: 520–700 $kgCO_2$eq/kWp for crystalline-silicon PV modules, based on the updated life-cycle inventory data compiled by the Photovoltaic Power Systems Programme Task 12 of International Energy Agency (IEA PVPS) [52]; 100–200 $kgCO_2$eq/kWh for Li-ion batteries for stationary applications, derived from the systematic reviews of Baumann et al. [53] and Peters et al. [54]; 150–200 $kgCO_2eq/m^2$ for flat-plate solar-thermal collectors, following Ardente et al. [55]; and 20–40 $kgCO_2$eq/kWh_th for domestic hot water (DHW) thermal storage tanks, drawing on the comparative Life Cycle Assessment (LCA) of Berger et al. [56] and the recent findings of Psimopoulos et al. [57]. The embodied footprint of the battery is counted twice to reflect its one mid-life replacement within the 20-year project horizon, consistent with the battery replacement schedule already adopted in the economic model (*Section 2.6*). This screening estimate is not a full cradle-to-grave life-cycle assessment: it omits transport, installation, end-of-life and recycling stages. It nonetheless provides an order-of-magnitude bound on how embodied emissions might affect the environmental-benefit conclusions reported in *Section 4*, expressed there as a carbon payback time, the time required for operational CO_2 savings to offset the one-time embodied footprint.

2.8. Multi-objective optimisation framework

The optimal sizing of the integrated renewable system was determined through a multi-objective evolutionary optimisation based on NSGA-II [58], implemented entirely in Python within the function *nsga2_optimize()*.

The optimisation problem is formulated as a vector maximisation:

$$\max_{\mathbf{x}} \mathbf{F}(\mathbf{x}) = \begin{bmatrix} NPV(\mathbf{x}) \\ C_{el}(\mathbf{x}) \\ C_{th}(\mathbf{x}) \\ -C_{tot}(\mathbf{x}) \end{bmatrix} \tag{26}$$

subject to:

$$\begin{cases} 0 \leqslant P_{PV} \leqslant P_{PV}^{\max} \\ 0 \leqslant C_{batt} \leqslant C_{batt}^{\max} \\ 0 \leqslant A_{coll} \leqslant A_{coll}^{\max} \\ 0 \leqslant E_{th,\,store} \leqslant E_{th,\,store}^{\max} \end{cases} \tag{27}$$

where the decision vector $\mathbf{x} = [P_{PV}, C_{Batt}, A_{th}, E_{th,\,store}]$ includes the rated PV power [kW_p], the battery energy capacity [kWh], the solar-collector area [m^2], and the thermal storage capacity [kWh_{th}]. The four objective functions correspond respectively to:

i. The *NPV*, representing the overall economic profitability;
ii. the electrical self-sufficiency index (C_{el}), i.e. the fraction of the electrical demand covered by PV and battery;
iii. the thermal self-sufficiency index (C_{th}), defined analogously for the thermal subsystem; and

iv. the negative of the total investment cost ($-C_{tot}$), allowing minimisation of capital expenditure within the same maximisation framework.

The optimisation bounds for both grid-connected and fully renewable configurations are reported in . Each candidate solution is evaluated by the deterministic simulation engine (*simulate_energy_system()*), while the NSGA-II relies on stochastic evolutionary operators under elitism and Pareto-based ranking. All simulations are executed with a fixed random seed, ensuring full reproducibility of the resulting Pareto fronts.

The initial population is generated through Latin Hypercube Sampling (LHS) [59], ensuring the uniform coverage of the multidimensional decision space and reducing initialisation bias. At every generation, individuals are ranked using the fast non-dominated sorting procedure [58]. Within each Pareto front, the crowding distance metric, as defined in the original NSGA-II formulation [58], quantifies the local density of solutions and preserves diversity along the front.

Parent selection is performed by binary tournament, favoring individuals with better rank and higher crowding distance. Offspring are produced via Simulated Binary Crossover (SBX) [60] and polynomial mutation [61]. Elitism is enforced by each generation so that all non-dominated individuals survive, ensuring a monotonic improvement of the Pareto front. All algorithmic settings are summarized in *Section S2.6* of *Supplementary Material*.

The algorithm proceeds for a fixed number of generations. The final output consists of a set of Pareto-optimal configurations, each representing a trade-off between economic profitability and energy self-sufficiency. Three representative designs are then extracted from each Pareto front: the configuration maximizing NPV (Best-NPV), the lowest-CAPEX solution achieving at least 95% of the maximum NPV (MinCAPEX-95NPV), and the solution maximizing the combined energy autonomy ($C_{el} + C_{th}$) (Best-coverage).

2.9. Performance indicators

This study adopts a consistent set of performance indicators computed directly from the hourly balances. Electrical self-sufficiency C_{el} [%] is defined as:

$$C_{el} = 100\cdot\left(1 - \frac{E_{imp,y}}{E_{load,y}}\right) \tag{28}$$

where $E_{imp,y}$ [kWh] is the yearly grid import and $E_{load,y}$ [kWh] is the yearly electrical demand. Thermal self-sufficiency C_{th} [%] is:

$$C_{th} = 100\cdot\left(1 - \frac{Q_{sol,\,y}}{Q_{th,\,load\,y}}\right) \tag{29}$$

where $Q_{sol,\,y}$ [kWh$_{th}$] is the useful solar heat delivered (directly and from storage) and $Q_{th,\,load}$ [kWh$_{th}$] is the yearly thermal requirement of the MD unit. Techno-economic indicators include C_{tot}, NPV, IRR, and DPBT, as defined in *Section 2.6*. The carbon benefit is monetized and integrated directly into the NPV in accordance with the environmental model (see *Section 2.7*). Battery cycling behaviour is tracked through the equivalent full cycles per year, as defined in Equation (16), which supports degradation and replacement cost analyses without influencing dispatch decisions. All indicators are evaluated deterministically by the simulation engine (*simulate_energy_system()*), ensuring perfect consistency with the energy balances of the PV, battery, and thermal subsystems.

Beyond these discounted-cash-flow indicators, the levelized cost of $Mg(OH)_2$ production is used to translate the economic benefit of renewable integration into process-economics terms, following the approach of Scelfo et al. [13]. Because the Best-NPV renewable configuration is sized primarily as a grid-export asset rather than dedicated process infrastructure (*Section 4.1*), only the share of the whole renewable-system capital expenditure (PV, battery, solar-thermal collectors and thermal storage) - rather than its full cost - proportional to the fraction of renewable generation actually self-consumed by the process is added to the capital expenditure of the CARMEn process chain itself [13]; this mirrors how shared infrastructure costs are conventionally apportioned between distinct outputs in proportion to usage. Because this self-consumption share is itself an outcome of the optimisation rather than a fixed input, a single value averaged across the Best-NPV configurations of the three scenarios (reported in *Section 4.2*) is applied uniformly for simplicity. Consistent with this allocation logic, revenue from exported electricity is not credited in the LCOMg calculation, avoiding double-counting the benefit of the renewable investment and mirroring its exclusion from the operational CO_2 accounting (*Section 2.7*).

While the LCOMg indicator translates the economic benefit of the Best-NPV design into a single process-economics figure, it does not by itself identify which subsystems and design choices actually drive that benefit across the wider design space. To address this, the full grid-connected Pareto front of each scenario (150 non-dominated solutions) was further analysed post-hoc, complementing the descriptive reporting of key Pareto-optimal solutions (*Section 4.1*). Pairwise Pearson correlations between the four objectives were computed to characterize objective conflicts across the front. Each objective was additionally regressed on the four standardized (z-scored) decision variables via ordinary least squares; the regression coefficients are standardized, meaning they are directly comparable and indicate the relative influence of each decision variable on the objective, while controlling for the mutual correlation of the variables along the front. To extend this driver analysis to fair cross-scenario comparisons, scenario comparisons in *Section 4.1* are further normalised by process load (thermal-to-electrical load ratio, and CO_2 avoided per unit of total energy demand), separating genuine differences in system efficiency from differences that simply reflect scenario size.

2.10. Sensitivity and uncertainty analysis protocol

A sensitivity analysis was conducted to assess the robustness of the optimal solutions to variations in external economic. The optimisation process was re-run for each perturbed scenario while keeping all decision-variable bounds and techno-economic inputs unchanged. Three sensitivity axes were analysed:

- *Export electricity tariff* – five representative scenarios were defined to reflect the range of regulatory frameworks governing remuneration of electricity exported to the Italian grid. Rather than varying an abstract price level, each scenario corresponds to a specific market or incentive scheme:

$$p_{SSP} \in \{0.086,\ 0.108,\ 0.140,\ 0.173,\ 0.216\}\quad €/\text{kWh}$$

These values correspond respectively to pessimistic market conditions, the baseline market condition based on 2024 (Sicilian day-ahead prices, Prezzo Unico Nazionale - PUN) [62], the moderate above-market premium scenario, and partially and fully incentivised Renewable Energy Community configurations, the latter including incentive contributions of approximately 0.110 €/kWh [63]. In each case, the hourly export electricity tariff time series is generated by scaling a normalized 24-hour price shape derived from hourly PUN data for 2024 to each scenario level.

- *Battery CAPEX* – the specific investment cost of the lithium-ion battery was varied across a range reflecting current and projected market prices for industrial systems:

$$c_{batt} \in \{400,\ 300,\ 250,\ 200,\ 150,\ 100\}\quad €/\text{kWh}$$

The baseline value of 300 €/kWh reflects 2024 European industrial installation costs. The150 €/kWh point represents the projected break-even threshold in the European context, expected as manufacturing scale-up continues to drive costs down towards the early 2030s [64].

- *Thermal energy value* – the reference cost of displaced thermal energy was varied to reflect uncertainty in backup fuel cost [65]:

$c_{th} \in \{0.07,\ 0.10,\ 0.13,\ 0.16,\ 0.20\}\ \ €/kWh_{th}$

For each perturbed scenario, a full NSGA-II optimisation is executed with identical algorithm settings, as reported in .

To complement the deterministic sensitivity analysis above, which re-optimises the design under discrete perturbed scenarios, a Monte Carlo uncertainty analysis was additionally performed to test the robustness of the already-identified Best-NPV grid-connected design under continuous, stochastic variation in its two most influential inputs. Rather than re-running the full NSGA-II optimisation, the already-optimised sizing (PV, battery, solar-thermal and thermal-storage capacities) was held fixed and re-evaluated via the deterministic simulation engine across 1000 independent draws per scenario. Each draw jointly samples (i) an annual solar-resource scaling factor, applied to both the PV and solar-thermal hourly production series (Normal distribution, mean 1.0, standard deviation 5%, reflecting typical inter-annual TMY-vs-actual solar-resource variability at Mediterranean sites [66]), and (ii) an export-tariff scaling factor, applied to the SSP profile (Uniform distribution, 0.8-1.3×, matching the range spanned by the five deterministic export-tariff scenarios above). This tests whether the recommended design remains viable under uncertainty, which is the practically relevant question for a reader deciding whether to build it, rather than asking how the optimal design itself would shift under different assumptions (already addressed by the deterministic sensitivity above). Results are reported in *Section 4*.

The three sensitivity axes - export tariff, battery capital cost, and thermal energy value - were selected as the parameters subject to the greatest near-term market and regulatory uncertainty over the 20-year horizon: the export tariff reflects Italy's evolving self-consumption and energy-community incentive schemes, battery capital cost is on a steep, well-documented decline curve without a comparable near-term analogue for the more mature PV technology, and thermal energy value tracks historically volatile natural-gas prices. Photovoltaic investment cost, collector degradation, the discount rate and the carbon-credit price were also considered; the latter was tested in an earlier iteration of this framework and excluded after proving to have a marginal effect (the monetised carbon credit accounts for only 3.8-6.6% of annual savings, since only self-consumed electricity is credited).

3. Case Study

This section defines the specific application of the framework described in *Section 2* to the CARMEn case. The reference site, climatic data, and three brine feed scenarios are presented first, followed by the full parametric setup (technical, economic, environmental, and algorithmic) used in all simulations and optimisation runs reported in *Section 4*.

3.1. Site and climatic data

Trapani (latitude 38.017°N, longitude 12.516°E), located on the western coast of Sicily, Italy, was selected as a representative Mediterranean location with high solar resource availability and strong practical relevance for industrial desalination and saltworks operations. From TMY data retrieved from the PVGIS database [29],Trapani features a semi-arid Mediterranean climate, with an annual Global Horizontal Irradiation (GHI) of 1842 kWh·m^{-2}, confirming its excellent suitability for solar-driven desalination and resource recovery [67]. Based on the TMY statistical analysis performed in this study, the daily-average ambient temperature ranges between 6.5°C in February to 31.6°C in August, reflecting mild winters and hot summers. Fig. 3 reports the daily mean irradiance profiles derived from the TMY data, showing a clear seasonal pattern with summer maxima and winter minima; the predominance of DNI over DHI in summer indicates predominantly clear-sky conditions, consistent with a semi-arid Mediterranean climate.

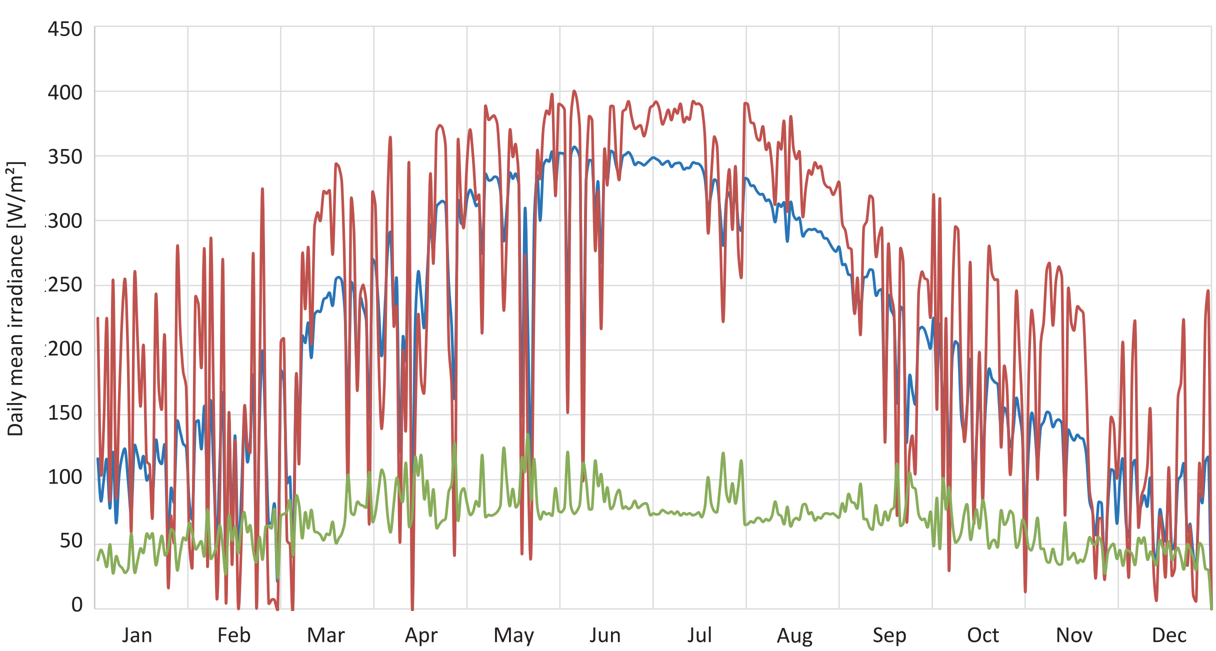

[W/m²]	Mean	Std	Min	Max
GHI	210.26	296.03	0	1022
DNI	234.29	316.68	0	991.54
DHI	67.63	86.56	0	457

Fig. 3. Daily mean irradiance profiles derived from PVGIS TMY data for Trapani (Italy) [29].

3.2. Feed scenarios and operating conditions

Three representative brine feed scenarios were analysed, corresponding to the three process configurations considered in the CARMEn chain: RO brine, NF retentate, and saltworks bittern. Although all three scenarios share the same annual $Mg(OH)_2$ production target of 50 t·y^{-1}, they differ markedly in feed composition, magnesium concentration, hydraulic throughput and, consequently, in the electrical and thermal energy demands imposed on the renewable energy system. All scenario definitions and process parameters are derived from the techno-economic study by Scelfo et al. [27], considering operating pH values of 10.6 for both RO brine and NF retentate, while 12 for bittern. These values correspond to the conditions exhibiting the lowest levelized cost of $Mg(OH)_2$ production.

The renewable system is sized and dispatched under continuous 24/7 operation using flat electrical and thermal load profiles specific to each scenario.

- *Scenario 1 – RO brine*: RO brine is the least concentrated feed considered (Mg^{2+} concentration of ~2.0 g/L) and therefore requires the largest processing volumes to achieve the same $Mg(OH)_2$ output. The corresponding large MD membrane area results in the highest thermal demand (42.36 kW_{th}) among the three scenarios.
- *Scenario 2 – NF retentate*: NF retentate scenario assumes that the RO brine is pre-concentrated through a nanofiltration step, enriching the Mg^{2+} content to ≈3.7 g/L and reducing scaling precursors before entering the precipitation and softening stages. Its thermal demand falls to ≈31 kW_{th} but the NF stage introduces an additional dedicated electrical load (≈4.4 kW), making this the most electrically demanding scenario of the three.
- *Scenario 3 – Bittern:* Saltworks bittern is the most concentrated feed, characterized by a very high magnesium content (≈49 g/L) and significantly reduced volumetric flowrates. It is the least energy-intensive scenario in both the electrical and thermal terms, with a thermal demand of only 7.84 kW_{th}.

The unit sizing of each process stage - precipitation reactor, softening resin, EDBM triplets, MD membrane area and RED stack - follows directly from these feed characteristics and is reported in full by Scelfo et al. [27]. The steady-state operating conditions for each scenario, used as inputs to the simulation framework, are summarised in Table 1. Thermal loads are computed from the process mass flow rate value of Table 1, and assuming a specific heat capacity of 4.05 kJ•(kg•K)$^{-1}$ and inlet and outlet feed temperature of $T_{feed,\ in} = 45°C$ and $T_{feed,\ out} = 20°C$.

Electrical load values are net of on-site reverse electrodialysis self-generation. RED gross power output is small relative to total process demand: approximately 90-106 W for RO brine, 46 W for NF retentate and 13-25 W for Bittern (0.5%, 0.21% and 0.09% of the reported electrical load, respectively; Scelfo et al. [13]) - a negligible contribution that does not materially affect the reported electrical demand regardless of the netting convention adopted.

3.3. Model parametrisation

The technical, economic, environmental and algorithmic parameters adopted for all simulations and optimisation runs are reported in full in Supplementary Section *S2* [68–77]. These comprise the decision-variable bounds (*Table S1*), the PV, solar-thermal collector and storage technical coefficients (*Table S2*), the techno-economic baseline reflecting 2024 Italian cost levels (*Table S3*), the dispatch and storage settings (*Table S4*), and the NSGA-II algorithmic configuration (*Table S5*), together with the software environment, hardware specifications and computational cost of each optimisation run. Three parameter choices are recalled here because they are referenced directly in the discussion of results: the baseline battery capital cost of 300 €/kWh, reflecting 2024 European industrial installation costs; the upper bound of 350 kW_p on PV peak power, corresponding to the maximum installable capacity given a roof area of 3000 m^2 at a specific footprint of 6 m^2/kW_p; and the scenario-dependent lower bound on battery capacity, set to guarantee three hours of autonomy at nominal load (54.6, 64.9 and 46.1 kWh for RO brine, NF retentate and Bittern respectively).

Table 1
Scenario definitions (continuous operation, $T_{feed,\ in} = 45°C$, $T_{feed,\ out} = 20°C$).

Scenario	Electric load	Thermal load	Mass flow rate
	[kW]	[kW]	[kg/s]
RO brine	18.21	42.36	0.418
NF retentate	21.63	31.08	0.307
Bittern	15.36	7.84	0.077

4. Results and discussion

This section presents and discusses the optimisation results obtained for the three brine feed scenarios under both grid-connected and fully renewable operating modes. Pareto-front analysis and the characterisation of best-trade-off configurations are reported first (Section 4.1), followed by economic performance and sensitivity analysis (Section 4.2), an assessment of the robustness of these results to input uncertainty and to the scope of the environmental accounting (Section 4.3), and a comparative assessment of grid-connected versus fully renewable solutions (Section 4.4). The section closes with a discussion of the main modelling limitations and their implications for the interpretation of the results (Section 4.5).

4.1. Grid-connected optimal configurations

The multi-objective NSGA-II optimisation yields well-distributed Pareto fronts for all three scenarios under grid-connected operation, spanning a broad range of configurations from minimal investment to near-maximum renewable coverage (see Fig. 4). The trade-off between NPV and combined energy autonomy ($C_{el} + C_{th}$) shows a consistent pattern across scenarios: NPV peaks at intermediate coverage levels and declines as autonomy increases, reflecting the diminishing economic returns of additional storage investment under baseline export tariff conditions. The three representative designs extracted from each front – Best-NPV, MinCAPEX-95NPV and Best-coverage – are discussed below.

Across all scenarios, the Best-NPV configuration consistently converges to a PV field at or near the upper bound (342-349 kWp), a battery dimensioned exclusively for 3-hour resilience minimum (46-65 kWh), and a solar-thermal field sized to achieve economically justified coverage without reaching the optimisation bound. This convergence reveals a clear economic logic: under baseline market conditions ($p_{SSP} = 0.108\,€/kWh$), exporting PV surplus to the grid is more valuable per kWh than storing it for later self-consumption, so the optimizer maximizes PV capacity while keeping battery size at the resilience floor. The near-identical PV sizing across all scenarios (342-349 kWp) is not coincidental but reflects the saturation of the upper bound, which is governed by the available roof area (3000 m^2, at 6 m^2/kWp) rather than by process load: under baseline market conditions, installing additional PV capacity is always economically advantageous regardless of scenario, since surplus generation is remunerated via grid export. The scenario-dependent differentiation therefore manifests not in PV sizing but in battery capacity, solar-thermal field and, consequently, in NPV and thermal coverage. The resulting export-driven dispatch behaviour is illustrated in the hourly energy profiles of Fig. 5. This pattern indicates that, at the economically optimal sizing found here, the PV subsystem operates less as a dedicated process-energy supply and more as a grid-export-oriented asset that happens to be co-located with the process: direct on-site consumption, while real, is a secondary rather than primary driver of its size. The system is accordingly best characterised as an

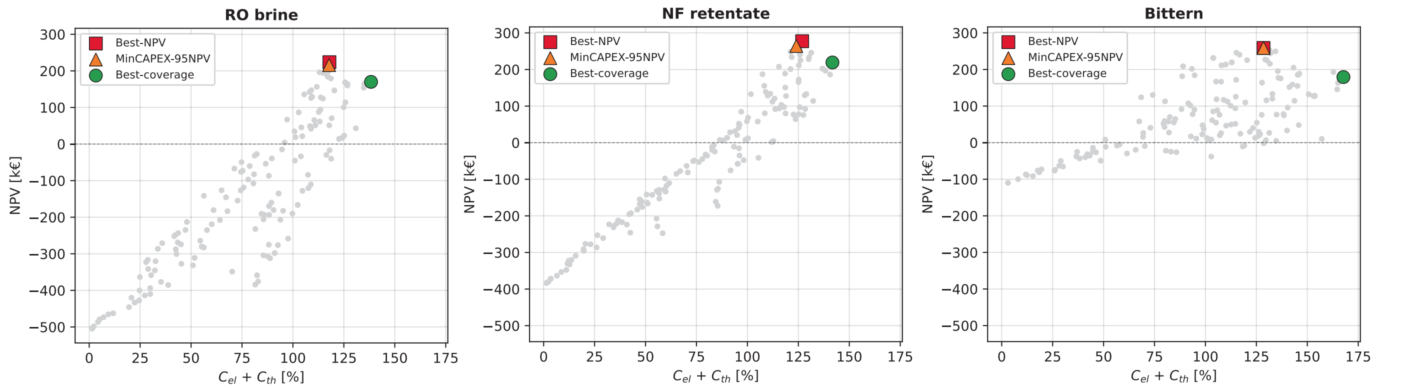

Fig. 4. Pareto fronts for the three scenarios under grid-connected operation. Each point represents a non-dominated design; three extracted representative solutions are highlighted: Best-NPV (■), MinCAPEX-95NPV (▲), and Best-coverage (●).

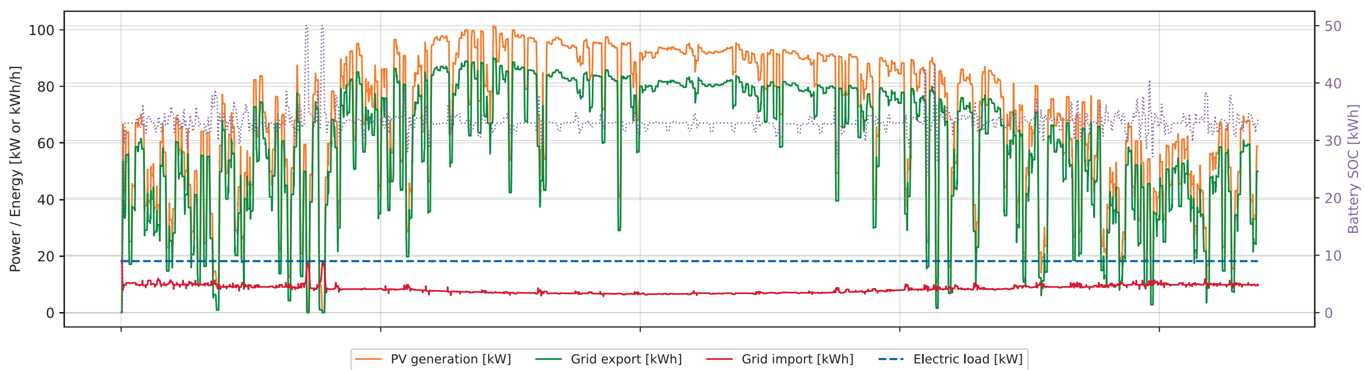

(a)

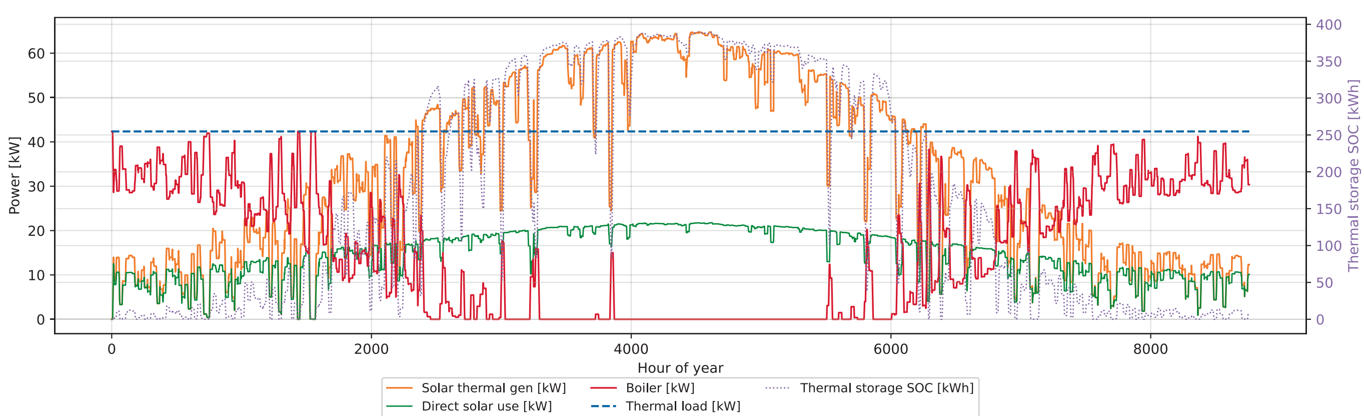

(b)

Fig. 5. Hourly energy profile (24 h rolling average) for the Best-NPV grid-connected solution of the RO brine scenario: (a) electrical subsystem showing PV generation, grid export and grid import against process load; (b) thermal subsystem showing solar-thermal generation, boiler backup, and thermal storage state of charge.

integrated process-and-export configuration rather than a purely process-driven one.

Table 2 reports annual energy balances for the Best-NPV configurations. The PV system delivers a specific yield of 1775.6 kWh/kWp in all three scenarios, consistent with the high solar resource available at the Trapani site (GHI=1841.8 kWh/m^2/y) and providing an implicit validation on the PV model against expected Mediterranean performance benchmarks, differences in annual PV production among scenarios are entirely attributable to the marginal variation in installed capacity rather than to site or model conditions. The dominant energy flow in all scenarios is grid export, which absorbs 83-88% of annual PV production against a direct self-consumption of only 10-14%, confirming the export-driven nature of the optimal dispatch under baseline market conditions. Battery throughput is modest by design, reflecting the small capacity sized at the minimum resilience bound.

On the thermal side, the balance is markedly scenario dependent. For RO brine, solar heat generation falls short of the thermal even at the economically optimal field size of 251 m^2, leaving 132.8 MWh/y to the auxiliary gas boiler; a direct consequence of the economic saturation of solar-thermal investment discussed in Section 4.2. NF retentate, by

Table 2
Annual energy balances for Best-NPV configurations (grid-connected).

	RO brine	NF retentate	Bittern
Electrical subsystem			
PV production [MWh/y]	607.3	616.1	619.6
PV specific yield [kWh/kWp/]	1775.6	1775.6	1775.6
PV self-consumed [MWh/y]	72.1	84.8	61.4
Battery discharge [MWh/y]	13.6	15.8	11.3
Grid export [MWh/y]	519.8	513.4	545.3
Grid import [MWh/y]	73.5	88.5	61.5
Export/PV production [%]	85.6	83.3	88.0
Thermal subsystem			
Solar heat generated [MWh/y]	289.5	316.9	81.5
Solar heat delivered to the chain [MWh/y]	238.2	200.9	51.1
Curtailed heat [MWh/y]	30.3	96.6	25.4
Storage thermal losses [MWh/y]	21.0	19.4	5.0
Boiler backup [MWh/y]	132.8	71.5	17.6

contrast, generates the largest solar heat volume but also the largest curtailment (96.6 MWh/y), its storage being unable to absorb the full summer surplus, while Bittern operates on a much smaller scale throughout. Storage standing losses remain consistent with the 2%/day rate assumed in the model.

Table 3 summarizes the key performance indicators for the Best-NPV solutions. NF retentate achieves the highest NPV despite its higher CAPEX, owing to a relatively large electrical load that maximizes PV self-consumption revenue and a moderate thermal demand that allows economically justified solar-thermal sizing without reaching the optimisation bound. RO brine achieves the lowest NPV, largely because its very high thermal demand (42.4 kW_{th}) requires a larger solar-thermal investment to maintain comparable coverage, while its lower electrical load per unit of PV capacity reduces the self-consumption benefit. Bittern achieves an intermediate NPV at the lowest CAPEX, reflecting its inherently simpler energy supply requirements.

Electrical self-sufficiency is remarkably consistent across scenarios, stabilising at 53-54%. This convergence reflects the saturation of PV capacity at the upper bound combined with a flat electrical load profile, which produces a near-constant ratio of generation to process demand regardless of scenario. Thermal coverage is instead scenario-dependent, ranging from 64.2% (RO brine) to 74.4% (Bittern). The lower value for RO brine confirms that its thermal demand approaches the economic saturation point for solar-thermal investment: beyond 251 m^2, the additional capital expenditure is not recovered through displaced gas boiler costs within the project lifetime. This sub-linear scaling of thermal coverage with thermal load is further discussed in *Section 4.2*.

From an environmental perspective, the Best-NPV configurations avoid between 37.8 t/y (Bittern) and 85.4 t/y (RO brine) of CO_2 equivalent annually. The breakdown between electrical and thermal contributions reveals a clear scenario-dependent pattern: for RO brine,

Table 3
Best-NPV solution key performance indicators (grid-connected).

Indicator	RO brine	NF retentate	Bittern
PV peak power [kWp]	342	347	349
Battery capacity [kWh]	56	65	46
Solar-thermal area [m^2]	251	275	71
Thermal storage [kWh_{th}]	602	436	115
CAPEX [k€]	647	652	514
NPV [k€]	224	277	259
IRR [%]	11.5	11.2	11.0
DPBT [years]	7.7	7.9	7.89
C_{el} *[%]*	53.7	53.1	54.1
C_{th} *[%]*	64.2	73.8	74.4
Service level elec. [%]	100	100	100
Service level th. [%]	100	100	100
Battery equivalent cycles[y^{-1}]	244.2	244.0	244.7
CO_2 *avoided – electrical [t/y]*	30.6	36.0	26.0
CO_2 *avoided – thermal [t/y]*	54.8	46.2	11.8
CO_2 *avoided – total [t/y]*	85.4	82.2	37.8

the thermal share dominates (64% of the total), reflecting the large solar-thermal field required to serve its high heat demand; for NF retentate, the split is more balanced, while for Bittern the electric contribution prevails, consistent with its very low thermal load (7.84 kW_{th}). These figures are computed excluding exported PV electricity from carbon accounting, in accordance with the conservative approach described in *Section 2.7*.

Battery cycling intensity is remarkably consistent across scenarios, with equivalent full cycles per year ranging narrowly between 244.0 (NF retentate) and 244.7 (Bittern). This near-identical cycling behaviour is a direct consequence of the small battery being sized at the 3-hour resilience minimum in all Best-NPV configurations: the limited capacity is fully exercised by the daily PV generation-demand mismatch, independently of the absolute load level. This metric confirms that the adopted sizing strategy imposes a uniform cycling regime across scenarios, with implications for lifetime estimation and replacement cost projections.

The MinCAPEX-95NPV solutions achieve 95% of the maximum NPV at meaningfully lower investment for NF retentate and RO brine (607 k€ and 628 k€ respectively), primarily by reducing PV capacity and thermal area while maintaining the same battery size. For Bittern, the Best-NPV and MinCAPEX-95NPV solutions coincide, indicating that the optimizer has already identified a configuration where further cost reduction would disproportionally sacrifice NPV.

The Best-coverage solutions reveal the cost of pursuing high renewable autonomy within a grid-connected framework. Increasing electrical coverage from ≈ 54% to 69-90% requires battery capacity to grow from the resilience minimum to 198-270 kWh, at an NPV penalty of 54-79 k€ relative to the Best-NPV solution. Under current battery costs (300 €/kWh), this additional storage capacity is economically justified only if the operator places an explicit value on energy autonomy beyond what is captured by the NPV formulation.

4.1.1. Pareto-front structure and design drivers

Beyond the three representative solutions above, the structure of the full 150-point Pareto front reveals which design variables actually shape each objective. Contrary to what a four-objective trade-off might suggest, NPV is strongly and positively correlated with both CAPEX (r=0.81-0.89) and thermal coverage (r≈0.91) across all three scenarios: within the explored design space, greater investment yields greater NPV up to a point of diminishing returns, rather than the two being strictly opposed. Electrical and thermal coverage, in contrast, are essentially uncorrelated for Bittern and RO brine (r≈0 and r=0.15 respectively, neither significant) and only moderately coupled for NF retentate (r=0.44), confirming that the electrical and thermal subsystems are largely independent design axes. Standardized regression of each objective on the four decision variables (Fig. 6) shows that CAPEX is overwhelmingly determined by PV capacity (β=0.75-0.90, R^2≈1.00) rather than battery or thermal-side sizing; electrical coverage is jointly driven by PV and battery capacity, while thermal coverage is driven almost exclusively by collector area, with thermal storage playing a secondary role. The dominant driver of NPV is scenario-dependent: for RO brine and NF retentate, PV and thermal area contribute comparably, whereas for Bittern - the lowest-thermal-load scenario - NPV is driven almost entirely by PV capacity alone (β=0.97), with thermal-side variables contributing negligibly. This mirrors the embodied-carbon-payback asymmetry identified in Section 4.3 and reinforces that economics of Bittern reduce, in practice, to a PV-sizing problem. The decision variable themselves also reveal how the two storage technologies relate: across the Pareto front, battery and thermal-storage capacity are essentially uncorrelated in all three scenarios (r=-0.19 to -0.01, not economically meaningful), indicating that they are sized independently rather than substituting for one another, whereas thermal-storage capacity is strongly correlated with collector area (r=0.58-0.84); the two thermal-side components scale together as a single thermal subsystem decision, while the battery is sized on its own, resilience-driven logic largely decoupled from both.

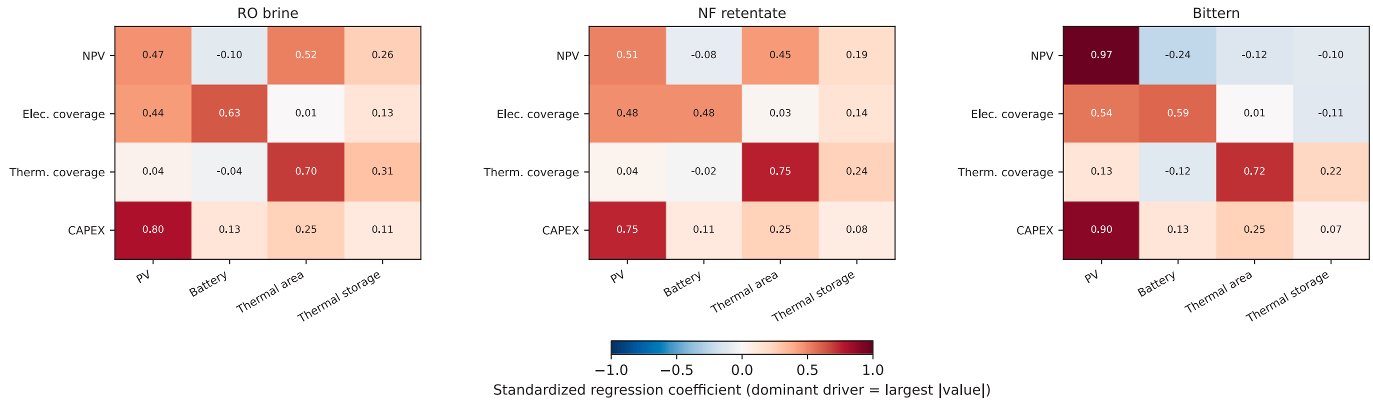

Fig. 6. Standardized regression coefficients ranking the influence of each decision variable (PV, battery, thermal collector area, thermal storage) on each objective (NPV, electrical coverage, thermal coverage, CAPEX), computed across the full 150-point grid-connected Pareto front for each scenario. Larger absolute values indicate a stronger influence; sign indicates direction.

Taken together, these results translate into concrete design guidance. Practitioners sizing a similar system should treat PV capacity, constrained by available roof area, as the primary design lever and expect it to saturate near that physical limit under baseline market conditions regardless of process scale. Battery capacity should be sized to the resilience requirement rather than enlarged for arbitrage, since it is only weakly linked to the other design variables and its own economics do not currently justify a larger role. Solar-thermal collector area and thermal-storage capacity should be sized together, as a single coupled decision, and scaled to the thermal-to-electrical load ratio of the process rather than to its absolute thermal demand.

4.1.2. *Physical drivers of inter-scenario differences*

The comparison across RO brine, NF retentate and Bittern is shaped primarily by one physical parameter: the thermal-to-electrical load ratio (2.33, 1.44 and 0.51 respectively; Table 1). Because Best-NPV PV capacity saturates near the same roof-area-limited bound in all three scenarios (see *Section 4.3*), this ratio, rather than absolute scenario size, determines how thermal or PV-dominated the economics and environmental profile of each scenario become. RO brine, with the highest ratio, requires the least collector area per unit of thermal load (5.9 m^2/kWth, vs. 8.8-8.9 for the other two scenarios) yet reaches the lowest thermal coverage (64.2% vs. 73.8% for both NF retentate and Bittern; Table 3); direct evidence of the economic saturation of solar-thermal investment. Capital efficiency (NPV per € invested) rises monotonically as the ratio falls: 0.346 for RO brine, 0.425 for NF retentate, 0.505 for Bittern (from the NPV and CAPEX values in Table 3). Bittern turns every euro of CAPEX into the most NPV of the three, because its low thermal load means its economics reduce to a near-PV-only sizing problem, consistent with the standardised-regression analysis above, where Bittern NPV driver is β=0.97 on PV capacity alone. The flip side is environmental: normalised per unit of total energy demand rather than reported in absolute terms, CO_2 avoided is actually highest for Bittern (0.185 t CO_2/MWh of demand, vs. 0.178 for NF retentate and 0.161 for RO brine): its lower absolute CO_2 avoided (37.8 vs. 82-85 t/y; Table 3) reflects having less total energy to decarbonise, not a less effective renewable integration, and its longer carbon payback (see *Section 4.3*) reflects the same fixed, roof-area-bound PV footprint being amortised against a smaller operational base.

4.2. *Economic performance and sensitivity analysis*

All three Best-NPV configurations are economically viable at baseline market conditions, with positive NPVs (224-277 k€), IRRs of 11.0-11.5%, and discounted payback times of approximately 8 years (Table 3). These results confirm that the integration of a hybrid PV-solar-thermal system with modest battery storage could deliver robust returns for circular brine-valorisation plants under current Italian market conditions, without requiring incentive schemes.

4.2.1. *Impact of renewable integration on the Levelized Cost of $Mg(OH)_2$ production*

Beyond pure energy economics, the renewable integration produces a meaningful reduction in the Levelized Cost of Magnesium Hydroxide production. As described in Section 2.9, allocating the whole renewable-system CAPEX, weighted by the self-consumption ratio (≈11% across scenarios), to the CARMEn process cost model [13] reduces the LCOMg by approximately 20% relative to the baseline without renewable integration: from 2.77 to 2.24 €/kg for RO brine, from 2.66 to 2.12 €/kg for NF retentate, and from 1.41 to 1.13 €/kg for saltworks bittern. This reduction is particularly significant for the bittern scenario, where the combination of the lowest process CAPEX and the smallest renewable system already delivers a LCOMg well below 1.5 €/kg even without incentive schemes, reinforcing its attractiveness as a near-term industrial configuration. By partially subsidising process capital through shared infrastructure, renewable integration materially improves the competitiveness of circular $Mg(OH)_2$ recovery against conventional supply chains.

4.2.2. *Export electricity tariff sensitivity*

The electricity export tariff is the dominant driver of economic performance across all scenarios (Fig. 7). At the pessimistic market scenario ($p_{SSP} = 0.086$ €/kWh), NPV remains positive (101-154 k€), confirming economic robustness even under adverse conditions. Under full CER incentive conditions ($p_{SSP} = 0.216$ €/kWh), NPV increases by 221-282% relative to baseline, reaching 845-902 k€. Critically, under these conditions, the hourly export tariff exceeds the grid import price (0.22 €/kWh) during peak hours, activating the hybrid dispatch override: the system shifts from a storage-priority to an export-priority strategy in those hours, further improving economic performance and qualitatively changing the optimal dispatch behaviour. The slope of the NPV-p_{SSP} curve is steeper for RO brine and NF retentate (which have larger PV fields relative to their electrical loads and therefore larger export volumes) than for Bittern.

4.2.3. *Battery CAPEX sensitivity*

At the current battery cost (300 €/kWh), the resilience constraint is the binding lower bound on battery sizing: removing it would reduce the optimal battery to near-zero capacity with a NPV gain of only 12-16 k€ (Fig. 8). This confirms that under current market conditions, battery storage in grid-connected systems is economically justified exclusively for resilience purposes. The break-even threshold (below which battery storage becomes economically attractive independently of the resilience constraint) is approximately 150 €/kWh for Bitter and RO brine, and

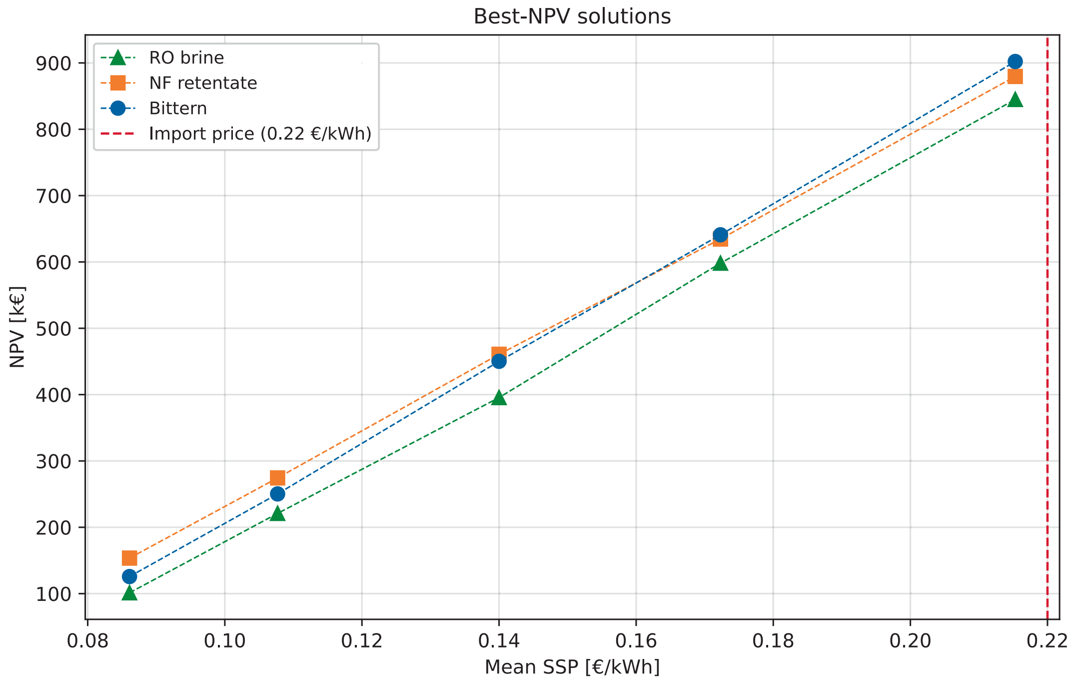

Fig. 7. Export tariff sensitivity across all scenarios.

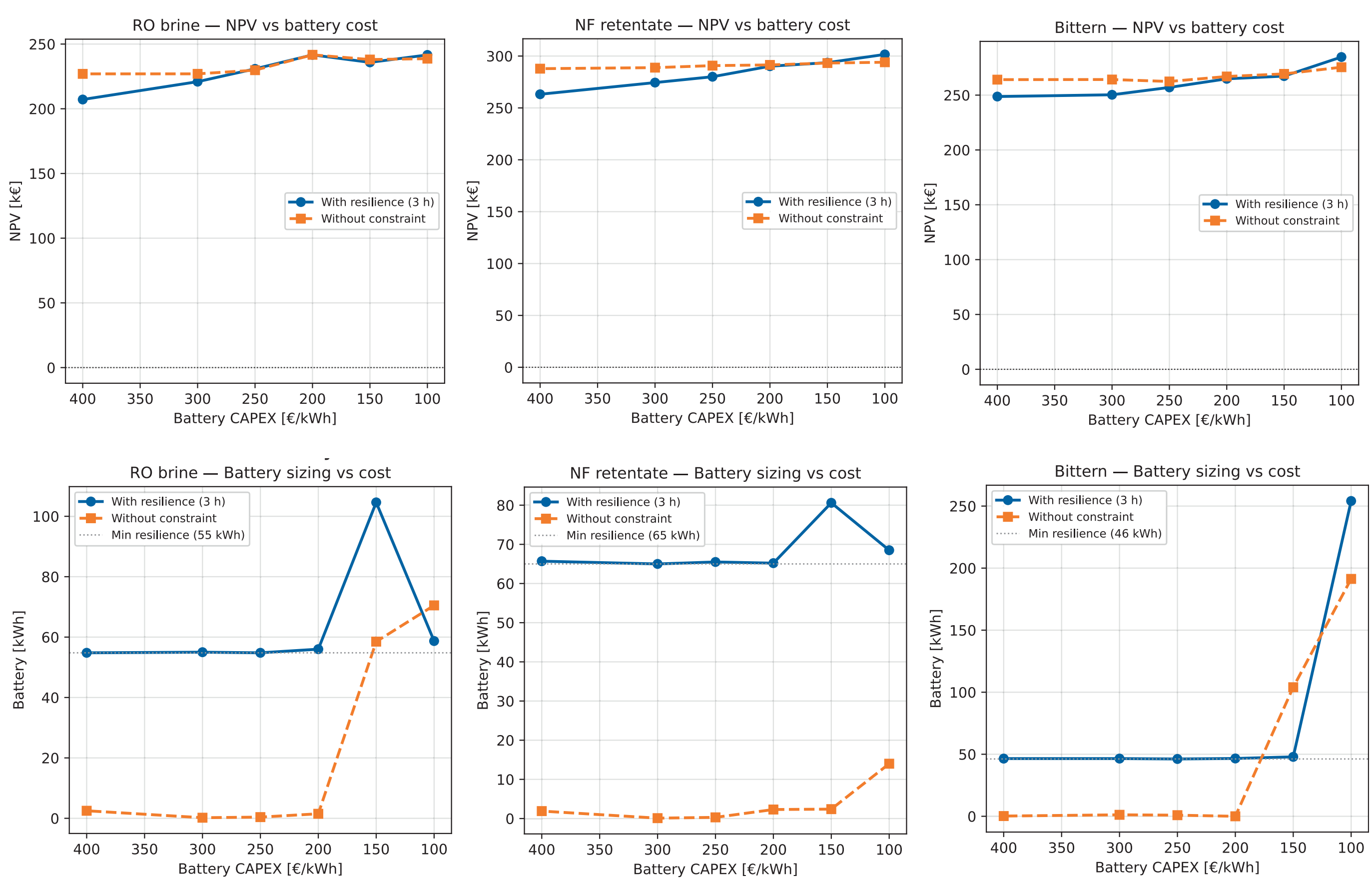

Fig. 8. Battery CAPEX sensitivity across all scenarios.

≈100 €/kWh for NF retentate. These thresholds are consistent with projected European market prices for industrial lithium-ion systems in the early 2030s [64], suggesting that the economic case for larger battery systems will strengthen significantly within the project lifetime.

4.2.4. *Thermal energy value sensitivity*

NPV increases approximately linearly with the reference thermal energy cost across all scenarios (Fig. 9), reflecting the direct proportionality between the value of displaced gas heat and the solar-thermal

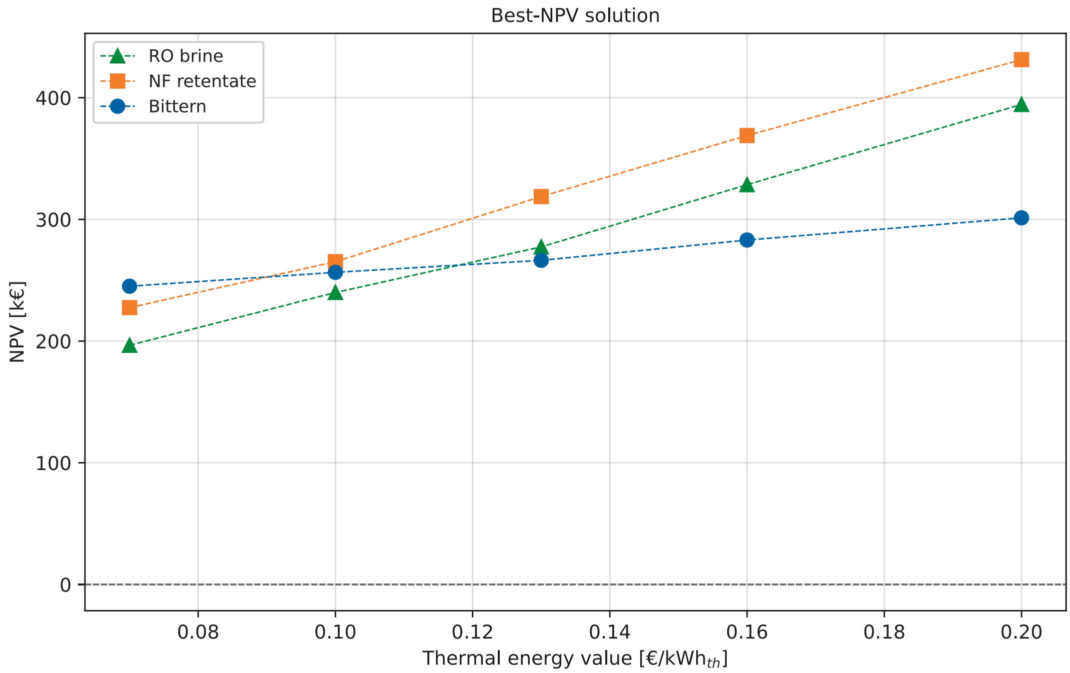

Fig. 9. Sensitivity of NPV to the thermal energy value across all scenarios.

benefit in the cash-flow model. NF retentate shows the steepest NPV-thermal value slope (+201 k€ over the range 0.07–0.20 €/kWh$_{th}$), followed by RO brine (+195 k€) and Bittern (+55 k€). A notable crossover occurs near the baseline thermal value (0.10 €/ kWh$_{th}$): below this threshold, Bittern yields the highest NPV owing to its low thermal CAPEX, while above it NF retentate becomes the most profitable scenario as its larger solar-thermal field generates proportionally greater savings on displaced gas costs. For RO brine, the optimal thermal area approaches the upper bound (≈250–296 m^2) across the full sensitivity range, meaning that the NPV sensitivity manifests primarily through economic returns rather than through changes in system sizing. For Bittern, the small thermal load (7.84 kW$_{th}$) means that both the optimal sizing (58–139 m^2) and the NPV respond strongly to gas price variations, even though in absolute terms the NPV gain remains modest.

4.3. Robustness to uncertainty and life-cycle scope

The analyses above establish the deterministic economic and environmental performance of the optimised designs. This subsection tests how far those conclusions can be trusted once three simplifications are relaxed: the assumption that solar resource and export price are known with certainty, the restriction of the environmental accounting to operational emissions only, and the use of a reduced computational budget for the sensitivity analyses in Section 4.2.

4.3.1. Robustness under solar-resource and price uncertainty

As described in Section 2.10, a Monte Carlo uncertainty analysis tests the robustness of the already-optimised Best-NPV grid-connected design of each scenario under combined solar-resource and export-tariff uncertainty. Across all three scenarios, economic viability proved robust to this combined uncertainty: none of the 3000 simulated draws yielded a negative NPV, with the 5th-percentile NPV remaining substantially positive in every case (83 k€ for RO brine, 143 k€ for NF retentate, 132 k€ for Bittern, against published deterministic values of 224 k€, 277 k€ and 259 k€ respectively; the Monte Carlo median is somewhat above the deterministic baseline in each case, reflecting the 1.05× mean of the uniform price-factor distribution rather than any bias in the underlying model). As Fig. 10 shows, the resulting NPV distributions are unimodal and comfortably clear of the break-even line for all three scenarios, and RO brine - the scenario with the lowest baseline NPV and thus the least economic headroom - is correspondingly the one whose distribution sits closest to, though still clearly separated from, zero; Bittern and NF retentate, with higher baseline NPV, show proportionally wider clearance from break-even. Electrical and thermal coverage were essentially insensitive to this uncertainty (within one percentage point of the deterministic value in all cases), as these are governed primarily by the

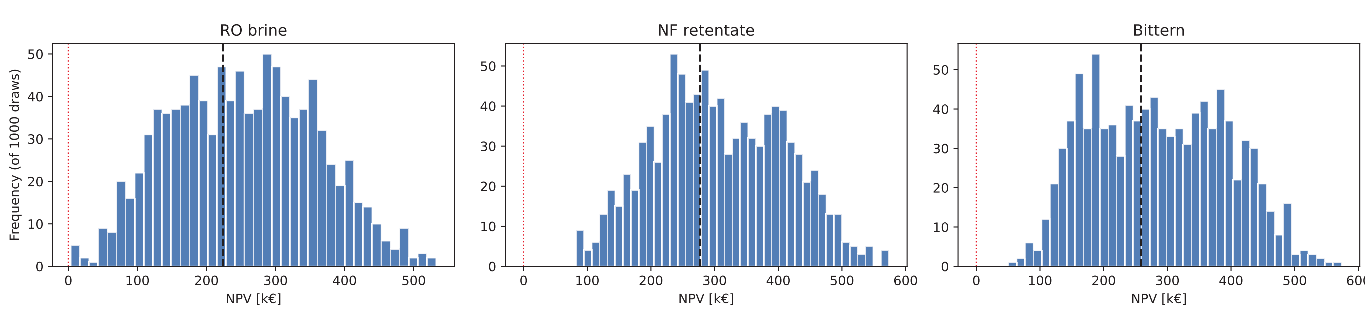

Fig. 10. Monte Carlo distribution of NPV under combined solar-resource (±5 % annual, Normal) and export-tariff (0.8–1.3×, Uniform) uncertainty for the Best-NPV grid-connected configuration of each scenario (1000 draws each). The dasched black line marks the published deterministic NPV; the dotted red line marks the break-even threshold (NPV = 0).

fixed sizing and load profile rather than by the perturbed solar resource or price. These results indicate that the reported economic viability is not an artefact of the deterministic TMY and price assumptions but holds under a realistic range of interannual solar-resource and market-price variability.

4.3.2. Screening-level embodied-emissions comparison

Section 2.7 described a screening-level estimate of the embodied emissions excluded from the operational-only environmental assessment above. Fig. 11 compares this one-time embodied footprint against the annual operational CO_2 avoided for the Best-NPV configuration of each scenario. The resulting carbon payback time, that is the time needed for operational savings to offset the embodied footprint, is 3.4 years for RO brine and 3.6 years for NF retentate, but 6.4 years for Bittern (with a plausible range of 5.4-7.5 years depending on the emission-factor assumptions used). This asymmetry follows directly from the sizing logic identified in Section 4.1: Best-NPV PV capacity saturates near the same roof-area-limited upper bound across all three scenarios, whereas the operational CO_2 avoided for Bittern is markedly lower due to its smaller thermal and electrical loads, so the (similarly sized) embodied PV footprint is proportionally harder to offset. Over the full 20-year project life, the net lifecycle carbon benefit remains clearly positive for all three scenarios: the embodied footprint amounts to 17-18% of cumulative operational savings for RO brine and NF retentate, and 32.1% for Bittern, confirming that the central environmental conclusion of this paper is not overturned by this exclusion, but the magnitude of the benefit is scenario-dependent and should be read with this qualification in mind, particularly for lower-load scenarios such as Bittern.

4.3.3. Convergence of the reduced NSGA-II setting used in the sensitivity analyses

The sensitivity analyses in *Section 4.2* use a smaller NSGA-II population/generation setting (60×60, or 40×50 for the thermal-energy-value sensitivity - see) than the 150×150 baseline, for computational tractability across the 5-6 parameter levels explored in each analysis. To confirm this does not compromise the comparability of the sensitivity conclusions with the baseline results, the grid-connected optimisation for RO brine, that is the scenario with the widest electrical/thermal trade-off, was re-run at the reduced 60×60 setting and compared against the published 150×150 Pareto front using the hypervolume indicator, a standard single-number multi-objective convergence metric. Fig. 12 shows the two fronts overlaid: the reduced setting retains 97.4% of the hypervolume of the baseline and identifies a best-NPV solution within 1.3% of the baseline optimum (220.9 vs. 223.8 k€), confirming that the reduced setting is sufficiently converged for the *Section 4.2* conclusions to be comparable with the baseline.

4.4. Grid-connected vs fully renewable

The comparison between grid-connected and fully renewable configurations reveals a fundamental economic asymmetry (Table 4, Fig. 13). All fully renewable configurations achieve near-complete electrical autonomy (99.9% C_{el}) but at an economic cost that renders them unviable under current market conditions: NPV is strongly negative (-1,061 to -1,261 k€) and the discounted payback time never materialises within the 20-year project lifetime.

The additional investment required for autonomous operation ranges from 566 to 739 k€ (87 - 113% above the grid-connected CAPEX), driven primarily by battery capacity, which increases by a factor of between 19.7 and 24.9 (from 46 - 65 kWh to 913 - 1,460 kWh). At current battery costs (300 €/kWh), battery CAPEX alone reaches 274 - 438 k€ in the fully renewable case - a 20-fold increase from the 14 - 20 k€ of the grid-connected resilience battery. Even at 100 €/kWh, battery investment would still reach 91- 146 k€, insufficient to recover economic viability.

A notable anomaly concerns thermal coverage in the fully renewable case. Despite much larger solar-thermal fields (up to 500 m^2) and thermal storage (up to 2000 kWh_{th}), thermal coverage for NF retentate (67.7%) and RO brine (82.3%) is lower than in the grid-connected case for NF retentate (73.8%), though higher than grid-connected for RO brine (64.2%). This apparently counter-intuitive result for NF retentate arises because the thermal field bound (500 m^2) proves insufficient to meet its large thermal demand (31 kW_{th}) throughout the winter period without gas boiler backup, which is unavailable in the fully renewable mode - unlike the grid-connected case where the boiler seamlessly covers residual deficits at no additional capital cost. Only Bittern, with its very low thermal load (7.84 kW_{th}), achieves near-complete thermal autonomy (98.6%) in the fully renewable configuration.

Achieving economic viability under full autonomy would require either external financing or battery costs well below 150 €/kWh - a threshold plausible within the project lifetime [64], but not yet reached in European markets.

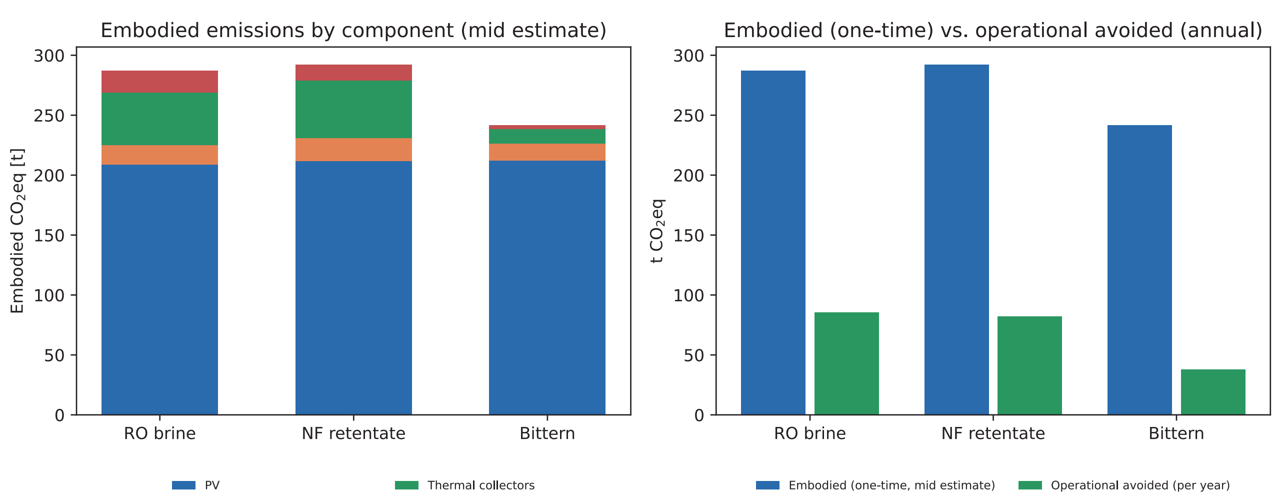

Fig. 11. Screening-level comparison of embodied manufacturing emissions: one-time, mid-estimate; PV, battery, including one replacement, solar-thermal collectors, thermal storage (left) against annual operational CO_2 avoided (right), for the Best-NPV grid-connected configuration of each scenario. Panels ordered: RO brine, NF retentate, Bittern.

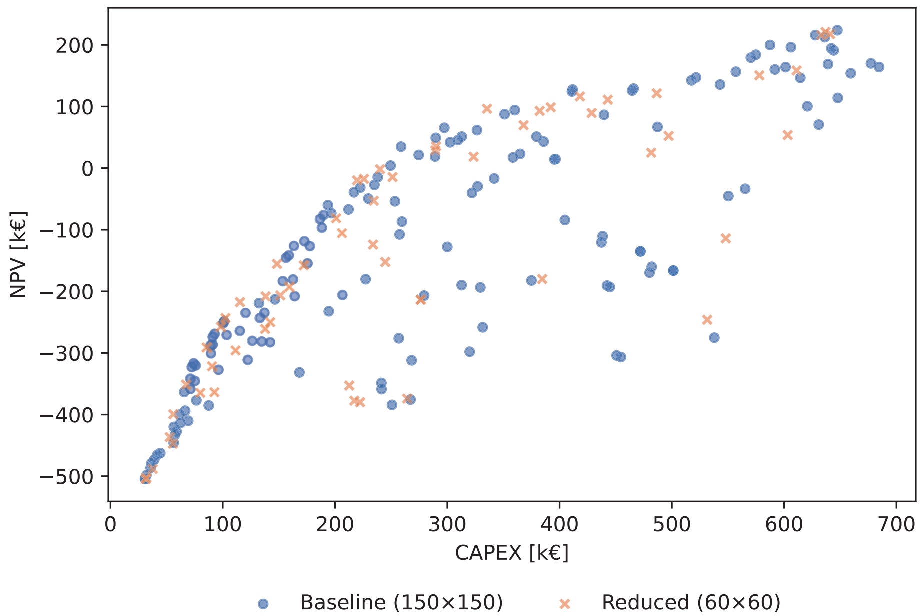

Fig. 12. Pareto front comparison for RO brine (grid-connected): baseline NSGA-II setting (150 × 150, circles) vs. the reduced setting used in the sensitivity analyses (60 × 60, crosses). The reduced setting retains 97.4 % of the hypervolume of the baseline and identifies a best-NPV solution within 1.3 % of the baseline optimum.

Table 4
Optimal system sizing for grid-connected (GC) vs fully renewable (FR): best-NPV solutions across the three feed scenarios.

	RO brine		NF retentate		Bittern	
	GC	FR	GC	FR	GC	FR
PV peak power [kWp]	342	316	347	552	349	513
Battery capacity [kWh]	56	1386	65	1,460	46	913
Solar-thermal area [m^2]	251	500	275	500	71	200
Thermal storage [kWh_{th}]	602	2000	436	2000	115	931

4.5. Limitations

While the results above demonstrate the economic viability across all three scenarios, several modelling choices bound the scope of these findings and are discussed here in turn: the dispatch strategy itself, the extent to which its robustness has been tested against uncertainty, the treatment of long-term economic parameters, and the assumption of perfect short-term foresight.

The framework relies on a deterministic, rule-based dispatch strategy rather than an optimal operational-scheduling formulation (e.g. model predictive control or mixed-integer linear programming). This choice is a direct consequence of the optimisation architecture: each candidate sizing is evaluated through a full 8760-hour dispatch simulation, repeated for every individual across 150 generations of a 150-member NSGA-II population (in the order of 10^4 full-year simulations per scenario). Embedding an hour-by-hour or rolling-horizon operational optimisation inside this outer sizing loop would increase the computational cost by orders of magnitude, making the four-objective co-design search intractable at the population and generation sizes used here. The resilience-first, look-ahead dispatch heuristic adopted instead is physically motivated (it reflects standard prosumer behaviour under reliability constraints) and is consistent with common practice in hybrid renewable energy sizing studies, where operational detail is deliberately traded off against the ability to explore a large design space. The reported economic performance should therefore be read as a conservative lower bound: a fully optimised operational schedule could only match or improve upon, not worsen, the dispatch outcomes obtained here, so the economic viability demonstrated in this study is unlikely to be an artefact of a suboptimal dispatch policy.

A related but distinct source of uncertainty is addressed empirically: a Monte Carlo analysis confirms that economic viability is preserved under realistic solar-resource (±5% annual) and export-price (0.8-1.3×) variability for the already-optimised designs. This analysis, however, does not cover two other deterministic assumptions: the process electrical and thermal loads are treated as fixed, continuous specifications

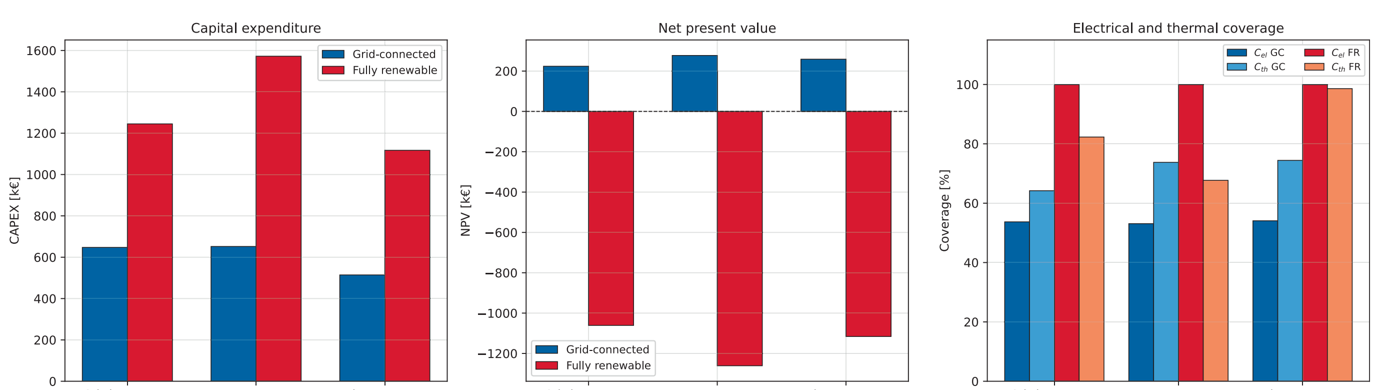

Fig. 13. Economic and energy performance comparison between grid-connected (GC) and fully renewable (FR) best-NPV configurations across the three scenarios.

inherited from the CARMEn process design rather than as stochastic operational variables, and PV performance degradation is modelled as a deterministic annual derating rather than as an uncertain rate, while solar-thermal collector performance is assumed constant over the project lifetime. Propagating uncertainty in load variability and degradation-rate assumptions and re-optimising the sizing itself under uncertainty, are natural extensions for future work.

Several economic parameters are held fixed by simplifying assumption: the grid electricity import tariff, operation-and-maintenance cost fractions, and the thermal energy value are held constant in real terms over the 20-year project horizon, a standard convention in discounted-cash-flow analysis that avoids compounding forecast uncertainty in inflation-adjusted commodity and service prices. The export tariff, the thermal energy value, and battery capital cost are test-stressed in *Section 4.2*, but the grid import tariff and the O&M fractions are not varied. Directionally, rising real electricity import prices (plausible given the ongoing European energy transition and its associated grid and carbon-price costs) would increase the value of self-consumption and therefore improve, not worsen, the reported economic performance; declining O&M costs, consistent with continued technology maturation for photovoltaic and battery systems, would have the same effect. The reported net present values should therefore be read as reflecting a conservative, present-day cost structure rather than a forecast of a specific future price trajectory.

A final idealisation concerns the operational information available to the dispatch algorithm itself: the 12-hour look-ahead of the battery dispatch assumes perfect foresight of future PV production, since it is computed directly from the already-known TMY rather than from a forecast. Real-world operation would instead rely on day-ahead irradiance and load forecasts subject to non-trivial error, particularly under partly-cloudy conditions; forecast error would be expected to degrade dispatch quality relative to the results reported here, most likely increasing grid reliance and reducing self-consumption at the margin, though quantifying this would require a dedicated forecast-error model and is left for future work.

5. Conclusions

This study presented a multi-objective optimisation framework for the integration of hybrid renewable energy systems (combining photovoltaics, battery storage, solar-thermal collectors and hot-water thermal storage) with the CARMEn circular brine valorisation chain, applied to a Trapani, Sicily case study. Three industrially representative feed scenarios (saltworks bittern, NF retentate and RO brine) were evaluated under both grid-connected and fully renewable operating modes, using NSGA-II with four simultaneous objectives: net present value, total CAPEX, electrical coverage and thermal coverage. The following conclusions can be drawn from the results.

Under grid-connected operation, economically viable configurations exist across all three scenarios at current Italian market conditions, without requiring incentive schemes. Best-NPV configurations consistently size the PV field near the upper design bound -and battery capacity at the 3-hour resilience minimum: NPV range from 224 k€ (RO brine) to 277 k€ (NF retentate), with IRRs of 11.0-11.5% and payback times around 8 years. Allocating the self-consumption share of renewable CAPEX to the process cost model reduces the levelised cost of Mg $(OH)_2$ production by approximately 20% relative to the CARMEn baseline without renewables- for all three scenarios. Thermal coverage -scales sub-linearly with thermal load, -reflecting economic saturation of solar-thermal investment beyond a scenario-specific threshold. The export tariff is the single dominant economic driver (NPV up 221-282% under full incentive conditions), while battery storage under current market costs is justified only for resilience, with a break-even investment threshold of roughly 100-150 €/kWh expected within the -project lifetime. Environmentally, avoided emissions range between 37.8 to 85.4 tCO_2/y across scenarios, with the thermal share dominating heat-intensive cases.

Fully renewable operation achieves near-complete electrical autonomy across all scenarios but is economically unviable under current conditions (NPV from -1,061 to -1,261 k€, no payback within the project lifetime), driven primary by a battery capacity requirements 19.7-24.9 times greater than the grid-connected case. A counter-intuitive -exception is that NF retentate achieves lower thermal coverage in fully renewable mode than when grid-connected, since the thermal field upper bound cannot buffer winter deficits without gas-boiler backup.

From a broader perspective, the results demonstrate that grid connection is not merely a cost-saving measure but a structural enabler of economic viability for solar-powered circular brine-valorisation systems at the scales considered. The hybrid renewable configuration analysed here, that includes large PV array, minimal resilience battery, moderate solar-thermal field, represents a robust design strategy for Mediterranean industrial sites seeking to reduce both operating costs and carbon footprint under current techno-economic conditions.

Future work should address the validation of simulated energy flows against measured data from a pilot installation, the extension of the optimisation framework to account for battery degradation and second-life scenarios, and the integration of demand-side flexibility through dynamic operation of the CARMEn process units, exploiting the growing number of hours with low or negative wholesale electricity prices expected under high renewable penetration.

CRediT authorship contribution statement

Stefania Guarino: Writing – review & editing, Writing – original draft, Software, Methodology, Formal analysis, Conceptualization. **Pietro Catrini:** Writing – review & editing, Validation, Formal analysis, Conceptualization. **Giuseppe Battaglia:** Writing – review & editing, Validation, Formal analysis, Conceptualization. **Giuseppe Scelfo:** Conceptualization. **Giorgio Maria Micale:** Supervision, Funding acquisition. **Livan Fratini:** Supervision, Funding acquisition.

Funding

This work was supported by the Made in Italy Circolare e Sostenibile (MICS) Extended Partnership, PNRR Project No. PE_00000004, funded by the European Union – NextGenerationEU.

Declaration of competing interest

The authors declare the following financial interests/personal relationships which may be considered as potential competing interests: Livan Fratini reports financial support was provided by European Union NextGenerationEU. If there are other authors, they declare that they have no known competing financial interests or personal relationships that could have appeared to influence the work reported in this paper.

Acknowledgement

This work was supported by the Made in Italy Circolare e Sostenibile (MICS) Extended Partnership PNRR Project No. PE_00000004) funded by the European Union NextGenerationEU

Declarations

Manuscript ECM-D-26-05915R1: "Multi-objective optimisation of renewable energy integration in circular brine valorisation/treatment: The case of the CARMEn chain".

Appendix A. Supplementary data

Supplementary data to this article can be found online at https://doi.org/10.1016/j.enconman.2026.122054.

Data availability

The meteorological data used in this study are publicly available from the Photovoltaic Geographical Information System (PVGIS) database, and the hourly electricity price data from the Gestore dei Mercati Energetici (GME) public archive. The process design and load data are taken from the published techno-economic study cited in the manuscript. The Python code implementing the optimisation model, the simulation algorithms and the sensitivity analyses is archived on Zenodo (doi: 10.5281/zenodo.20067429). The repository is currently under embargo; the authors will release the embargo upon acceptance and publication of the article, at which point the code will be freely accessible under an MIT license.

References

[1] He C, Liu Z, Wu J, Pan X, Fang Z, Li J, et al. Future global urban water scarcity and potential solutions. Nat Commun 2021;12:4667. https://doi.org/10.1038/s41467-021-25026-3.

[2] Eke J, Yusuf A, Giwa A, Sodiq A. The global status of desalination: An assessment of current desalination technologies, plants and capacity. Desalination 2020;495: 114633. https://doi.org/10.1016/J.DESAL.2020.114633.

[3] Rivero-Falcón Á, Peñate Suárez B, Melián-Martel N. SWRO Brine Characterisation and Critical Analysis of Its Industrial Valorisation: A Case Study in the Canary Islands (Spain). Water 2023;15. https://doi.org/10.3390/w15081600.

[4] Lee C-H, Ho H-J, Chen W-S, Iizuka A. Total Resource Circulation of Desalination Brine: A Review. Adv Sustain Syst 2024;8:2300460. https://doi.org/10.1002/adsu.202300460.

[5] Omerspahic M, Al-Jabri H, Siddiqui SA, Saadaoui I. Characteristics of Desalination Brine and Its Impacts on Marine Chemistry and Health, With Emphasis on the Persian/Arabian Gulf. A Review. Front Mar Sci 2022;Volume 9-. https://doi.org/10.3389/fmars.2022.845113.

[6] Panagopoulos A, Haralambous K-J. Minimal Liquid Discharge (MLD) and Zero Liquid Discharge (ZLD) strategies for wastewater management and resource recovery – Analysis, challenges and prospects. J Environ Chem Eng 2020;8: 104418. https://doi.org/10.1016/j.jece.2020.104418.

[7] Banerjee P, Zaneldin EK, Al-Marzouqi AH, Ahmed WK. A Review of Reject Brine Disposal, Management, and Construction Applications. Buildings 2025;15. https://doi.org/10.3390/buildings15132317.

[8] Caceres Gonzalez RA, Hatzell MC. Electrified Solar Zero Liquid Discharge: Exploring the Potential of PV-ZLD in the US. Environ Sci Technol 2024;58: 15562–74. https://doi.org/10.1021/acs.est.4c00494.

[9] European Commission. Critical raw materials n.d.

[10] Morgante C, Vassallo F, Cassaro C, Virruso G, Diamantidou D, Van Linden N, et al. Pioneering minimum liquid discharge desalination: A pilot study in Lampedusa Island. Desalination 2024;581:117562. https://doi.org/10.1016/j.desal.2024.117562.

[11] Miciletta F, Battaglia G, Scelfo G, Vassallo F, Vicari F, Tamburini A, et al. A Novel Pilot-scale Crystallizer for the Production of Mg (OH) 2 Powders from Saltworks Bitterns. Chem Eng Trans 2025;119:7–12.

[12] Scelfo G, Serrano-Tari P, Raffaelli R, Vicari F, Oller I, Cipollina A, et al. The Operational Performance of an Ultrafiltration Pilot Unit for the Treatment of Ultra-Concentrated Brines. Membranes (Basel) 2024;14:276.

[13] Scelfo G, Battaglia G, Cardella M, Filingeri A, Culcasi A, Volpe F, et al. The CARMEn project: A sustainable and circular brine treatment chain. Desalination 2025:119641. https://doi.org/10.1016/j.desal.2025.119641.

[14] Herrero-Gonzalez M, Culcasi A, Tamburini A, Ibañez R, Cipollina A, Micale G. Techno-economic feasibility of photovoltaic solar electrodialysis with bipolar membranes. Desalination 2024;582:117624. https://doi.org/10.1016/j.desal.2024.117624.

[15] Herrero-Gonzalez M, Diaz-Guridi P, Dominguez-Ramos A, Ibañez R, Irabien A. Photovoltaic solar electrodialysis with bipolar membranes. Desalination 2018;433: 155–63. https://doi.org/10.1016/j.desal.2018.01.015.

[16] Cassaro C, Virruso G, Cipollina A, Fagiolini A, Tamburini A, Micale G. Enhanced Schemes for Brine Valorization via Electrodialysis with Bipolar Membranes Powered by Renewable Energy. ACS Omega 2025;10:10122–38. https://doi.org/10.1021/acsomega.4c08609.

[17] Wang W, Shi Y, Zhang C, Hong S, Shi L, Chang J, et al. Simultaneous production of fresh water and electricity via multistage solar photovoltaic membrane distillation. Nat Commun 2019;10:3012. https://doi.org/10.1038/s41467-019-10817-6.

[18] Amiruddin D, Mahajan D, Fang D, Wang W, Wang P, Hsiao BS. A Facile Ultrapure Water Production Method for Electrolysis via Multilayered Photovoltaic/Membrane Distillation. Energies 2023;16. https://doi.org/10.3390/en16155765.

[19] Fang D, Amiruddin DM, Kao I, Mahajan D, Chen X, Hsiao BS. Towards the Optimization of a Photovoltaic/Membrane Distillation System for the Production of Pure Water. Membranes (Basel) 2024;14. https://doi.org/10.3390/membranes14050110.

[20] Rabie M, Ali AYM, Abo-Zahhad EM, Elkady MF, El-Shazly AH, Salem MS, et al. New hybrid concentrated photovoltaic/membrane distillation unit for simultaneous freshwater and electricity production. Desalination 2023;559: 116630. https://doi.org/10.1016/j.desal.2023.116630.

[21] Bouguecha ST, Aly SE, Al-Beirutty MH, Hamdi MM, Boubakri A. Solar driven DCMD: Performance evaluation and thermal energy efficiency. Chem Eng Res Des 2015;100:331–40. https://doi.org/10.1016/j.cherd.2015.05.044.

[22] Gustafson RD, Hiibel SR, Childress AE. Membrane distillation driven by intermittent and variable-temperature waste heat: System arrangements for water production and heat storage. Desalination 2018;448:49–59. https://doi.org/10.1016/j.desal.2018.09.017.

[23] Hlal MI, Ramachandaramurthya VK, Padmanaban S, Kaboli HR, Pouryekta A, Bin TAR, et al. NSGA-II and MOPSO based optimization for sizing of hybrid PV/wind/battery energy storage system. Int J Power Electron Drive Syst 2019;10:463.

[24] Cheraghi R, Hossein JM. Multi-objective optimization of a hybrid renewable energy system supplying a residential building using NSGA-II and MOPSO algorithms. Energy Convers Manag 2023;294:117515. https://doi.org/10.1016/j.enconman.2023.117515.

[25] Bamisile O, Cai D, Adun H, Dagbasi M, Ukwuoma CC, Huang Q, et al. Towards renewables development: Review of optimization techniques for energy storage and hybrid renewable energy systems. Heliyon 2024;10:e37482. https://doi.org/10.1016/j.heliyon.2024.e37482.

[26] Ojo OE, Oludolapo OA. Innovative Recovery Methods for Metals and Salts from Rejected Brine and Advanced Extraction Processes—A Pathway to Commercial Viability and Sustainability in Seawater Reverse Osmosis Desalination. Water 2025;17. https://doi.org/10.3390/w17213141.

[27] Scelfo G, Charitopoulos VM, Vicari F, Tamburini A, Bogle DI, Micale G, et al. Surrogate-based optimization analysis and scale-up of an ultra-concentrated brine pilot treatment chain for sustainable mineral recovery. Desalination 2026;621: 119682. https://doi.org/10.1016/j.desal.2025.119682.

[28] Holmgren WF, Hansen CW, Mikofski MA. pvlib python: A python package for modeling solar energy systems. J Open Source Softw 2018;3:884.

[29] Photovoltaic Geographical Information System (PVGIS). Typical Meteorological Year n.d. https://re.jrc.ec.europa.eu/pvg_tools/en/#TMY.

[30] Jensen AR, Anderson KS, Holmgren WF, Mikofski MA, Hansen CW, Boeman LJ, et al. pvlib iotools—Open-source Python functions for seamless access to solar irradiance data. Sol Energy 2023;266:112092. https://doi.org/10.1016/j.solener.2023.112092.

[31] Hay JE. Calculation if the solar radiation incident on inclined surfaces. Proc. first Can. Sol. Radiat. Data Work. Toronto. Ontario, Canada 1978, 1978.

[32] Perez R, Seals R, Ineichen P, Stewart R, Menicucci D. A new simplified version of the perez diffuse irradiance model for tilted surfaces. Sol Energy 1987;39:221–31. https://doi.org/10.1016/S0038-092X(87)80031-2.

[33] Loutzenhiser PG, Manz H, Felsmann C, Strachan PA, Frank T, Maxwell GM. Empirical validation of models to compute solar irradiance on inclined surfaces for building energy simulation. Sol Energy 2007;81:254–67. https://doi.org/10.1016/j.solener.2006.03.009.

[34] King D, Boyson WE, Kratochvil JA. Sandia photovoltaic array performance model. SAND Rep 2004;3535.

[35] Anderson K, Kemnitz J, Boyd M. Evaluating cell temperature models and the effect of wind speed in PV system capacity testing. 2021 IEEE 48th Photovolt. Spec. Conf., 2021, p. 1663–9.

[36] Dobos AP. PVWatts Version 5 Manual. 2014. doi: 10.2172/1158421.

[37] Dobos AP. PVWatts Version 5 Manual. 2014. doi: 10.2172/1158421.

[38] Jordan DC, Kurtz SR. Photovoltaic degradation rates—an analytical review. Prog Photovoltaics Res Appl 2013;21:12–29.

[39] Jordan DC, Kurtz SR, VanSant K, Newmiller J. Compendium of photovoltaic degradation rates. Prog Photovoltaics Res Appl 2016;24:978–89.

[40] Gestore dei Servizi Energetici (GSE). Scambio sul posto n.d. https://www.gse.it/servizi-per-te/fotovoltaico/scambio-sul-posto (accessed October 22, 2025).

[41] Gestore dei Servizi Energetici (GSE). Configurazioni per l'autoconsumo diffuso n.d. https://www.gse.it/servizi-per-te/autoconsumo/gruppi-di-autoconsumatori-e-comunita-di-energia-rinnovabile/comunità-energetiche-rinnovabili.

[42] Cole W, Frazier AW, Augustine C. Cost projections for utility-scale battery storage: 2021 update. 2021.

[43] Lai CS, McCulloch MD. Levelized cost of electricity for solar photovoltaic and electrical energy storage. Appl Energy 2017;190:191–203. https://doi.org/10.1016/J.APENERGY.2016.12.153.

[44] Ferreira SKR, Rose DM, Schoenwald DA, Bray K, Conover D, Kintner-Meyer M, et al. Protocol for uniformly measuring and expressing the performance of energy storage systems. 2013.

[45] Anderson K, Olis D, Becker B, Parkhill L, Laws N, Li X, et al. REopt Lite user manual. 2021.

[46] Duffie JA, Beckman WA. Solar engineering of thermal processes. John Wiley & Sons; 2013.

[47] Dinçer I, Rosen MA. Thermal Energy Storage. Systems and applications. Wiley; 2011.

[48] Short W, Packey DJ, Holt T. A manual for the economic evaluation of energy efficiency and renewable energy technologies. 1995. doi: 10.2172/35391.

[49] NumPy. numpy-financial 1.0.0 n.d. https://numpy.org/numpy-financial/latest/ (accessed July 15, 2025).

[50] Yudin A. Essential financial tasks done with python. Basic Python Data Manag. Financ. Mark. Adv. Your Career by Learn. Most Powerful Anal. Tool, Springer 2021:231–75.

[51] Eggleston, H S; Buendia, L; Miwa, K; Ngara, T; Tanabe K. 2006 IPCC Guidelines for National Greenhouse Gas Inventories n.d.

[52] Wambach K, Libby C. Advances in Photovoltaic Module Recycling: Third Update to Empirical Life Cycle Inventory Data (Report No. T12-32:2026). 2025. doi: 10.69766/PJOW5359.

[53] Baumann M, Peters JF, Weil M, Grunwald A. CO2 Footprint and Life-Cycle Costs of Electrochemical Energy Storage for Stationary Grid Applications. Energy Technol 2017;5:1071–83. https://doi.org/10.1002/ente.201600622.

[54] Peters JF, Baumann M, Zimmermann B, Braun J, Weil M. The environmental impact of Li-Ion batteries and the role of key parameters–A review. Renew Sustain Energy Rev 2017;67:491–506.

[55] Ardente F, Beccali G, Cellura M, Lo BV. Life cycle assessment of a solar thermal collector. Renew Energy 2005;30:1031–54. https://doi.org/10.1016/j.renene.2004.09.009.

[56] Berger M, Zimmermann R-P, Felder T, Maranda S, Fischer LJ. Life cycle analysis of PCM-enhanced domestic hot water storage 2022.

[57] Psimopoulos E, Eriksson O, Bales C. Environmental and techno-economic assessment of energy storages in a single-family building with an exhaust air heat pump. Energy Build 2026;365:117659. https://doi.org/10.1016/j.enbuild.2026.117659.

[58] Deb K, Pratap A, Agarwal S, Meyarivan T. A fast and elitist multiobjective genetic algorithm: NSGA-II. IEEE Trans Evol Comput 2002;6:182–97. https://doi.org/10.1109/4235.996017.

[59] Mckay MD, Beckman RJ, Conover WJ. A Comparison of Three Methods for Selecting Values of Input Variables in the Analysis of Output From a Computer Code. Technometrics 2000;42:55–61. https://doi.org/10.1080/00401706.2000.10485979.

[60] Deb K, Agrawal RB, et al. Simulated binary crossover for continuous search space. Complex Syst 1995;9:115–48.

[61] Deb K, Goyal M, et al. A combined genetic adaptive search (GeneAS) for engineering design. Comput Sci Informatics 1996;26:30–45.

[62] Gestore dei Mercati Energetici (GME). MGP – Esiti: Prezzi zonali orari 2024 (Zona Sicilia) n.d. https://gme.mercatoelettrico.org/it-it/Home/Esiti/Elettricita/MGP/Esiti/PrezziZonali#IntestazioneGrafico (accessed September 22, 2025).

[63] Ministero dell'Ambiente e della Sicurezza Energetica (MASE). Decreto 7 dicembre 2023, n. 414 – Incentivi per l'energia da fonti rinnovabili prodotta da configurazioni di autoconsumo per la condivisione dell'energia rinnovabile (CACER). Gazzetta Ufficiale della Repubblica Italiana, Serie Generale n. 301, 27 dicembre 2023; n.d.

[64] International Energy Agency. Batteries and Secure Energy Transitions. Paris, France: 2024.

[65] Eurostat. Gas prices for non-household consumers – bi-annual data (from 2007 onwards) 2026.

[66] Suri M, Huld T, Dunlop E, Albuisson M, Lefèvre M, Wald L. Uncertainties in solar electricity yield prediction from fluctuation of solar radiation. 22nd Eur. Photovolt. Sol. Energy Conf. 2007.

[67] Calise F, Cappiello FL, Vanoli R, Vicidomini M. Economic assessment of renewable energy systems integrating photovoltaic panels, seawater desalination and water storage. Appl Energy 2019;253:113575.

[68] Kost, Christoph; Müller, Paul; Sepúlveda Schweiger, Jael; Fluri, Verena; Thomsen J. Levelized Cost of Electricity- Renewable Energy Technologies 2024.

[69] Han X, Garrison J, Hug G. Techno-economic analysis of PV-battery systems in Switzerland. Renew Sustain Energy Rev 2022;158:112028. https://doi.org/10.1016/j.rser.2021.112028.

[70] Weiss W, Spörk-Dür M. Solar heat worldwide. Global Market Development and Trends 2023. Detailed Market Figures 2022. Gleisdorf, Austria: 2024. doi: 10.18777/ieashc-shww-2024-0001.

[71] Clean Energy Technology Observatory, Novel thermal energy storage in the European Union – Status report on technology development, trends, value chains and markets – 2024. Publications Office of the European Union; 2024. doi: doi/10.2760/6320829.

[72] Eurostat. Electricity price statistics - Electricity prices for non-household consumers. first half 2025. Luxembourg: Publications Office of the European Union; 2025.

[73] Gestore dei Servizi Energetici (GSE). Scambio sul posto n.d.

[74] Beltran H, Ayuso P, Pérez E. Lifetime Expectancy of Li-Ion Batteries used for Residential Solar Storage. Energies 2020;13. https://doi.org/10.3390/en13030568.

[75] Gulkowski S, Díez JVM, Tejero JA, Dragan P, Nofuentes G. A Study on Long-Term Operation and Performance Loss Rates of Various PV Technologies in Eastern Poland. Renew. Energy 2025. 124548.

[76] ISPRA. Fattori di emissione per la produzione ed il consumo di energia elettrica in Italia 2025.

[77] European Union. Report from the commission to the european parliament and the councIL on the functioning of the European carbon market in 2023 2024.